

Identifying LISA verification binaries among the Galactic population of double white dwarfs

Eliot Finch¹,^{*} Giorgia Bartolucci,¹ Daniel Chucherko,¹ Ben G. Patterson,¹ Valeriya Korol^{1,2},
 Antoine Klein¹, Diganta Bandopadhyay¹, Hannah Middleton¹, Christopher J. Moore¹, and
 Alberto Vecchio¹

¹*Institute for Gravitational Wave Astronomy & School of Physics and Astronomy, University of Birmingham, Birmingham, B15 2TT, UK*

²*Max-Planck-Institut für Astrophysik, Karl-Schwarzschild-Straße 1, 85741 Garching, Germany*

Accepted XXX. Received YYY; in original form ZZZ

ABSTRACT

Double white dwarfs (DWDs) will be the most numerous gravitational-wave (GW) sources for the Laser Interferometer Space Antenna (*LISA*). Most of the Galactic DWDs will be unresolved and will superpose to form a confusion noise foreground, the dominant *LISA* noise source around $\sim 0.5\text{--}3$ mHz. A small fraction of these sources will stand out from the background and be individually detectable. Uniquely among GW sources, a handful of these binaries will be known in advance from electromagnetic (EM) observations and will be guaranteed sources of detectable GWs in the *LISA* band; these are known as verification binaries (VBs). High-cadence photometric surveys are continuously discovering new VB systems, and their number will continue to grow ahead of the launch of *LISA*. We analyse, in a fully Bayesian framework, all the currently known VB candidates with the latest design requirements for the *LISA* mission and find that 25 of the considered sources can be detected within a 4 yr observation time. We explore what can be expected from GW observations, both alone and in combination with EM observations, and estimate the VB’s time to detection in the early months of *LISA* operations. We also show how VBs can be analysed in the case where their GW signals compete with many other unknown binary signals (both resolved and unresolved) from a realistic Galactic population of DWDs.

Key words: gravitational waves – binaries: close – stars: individual: white dwarfs

1 INTRODUCTION

The Laser Interferometer Space Antenna (*LISA*) is a gravitational-wave (GW) observatory currently under development for science operations in the 2030s (Amaro-Seoane et al. 2017). The *LISA* design is optimised for sensitivity to GWs in the mHz range and the instrument will provide the first look at the GW sky in the frequency band $\sim 0.1\text{--}500$ mHz.

From the first inception of a mission concept aimed at the mHz GW spectrum (Danzmann et al. 1993), it was realised that the Galactic population (GP) of short-period ($\lesssim 1$ h) ultra-compact binaries (UCBs) – white dwarfs, neutron stars, and stellar-mass black holes – represented a copious reservoir of detectable GW sources (Lipunov et al. 1987; Hils et al. 1990). It is now clear that at *LISA*’s requirement sensitivity (Babak et al. 2021) the instrument will be able to individually resolve tens of thousands of these UCBs (Amaro-Seoane et al. 2023). Galactic double white dwarfs (DWDs), both detached and interacting, will constitute the overwhelming majority of detected UCBs (Nelemans et al. 2004; Nissanke et al. 2012; Korol et al. 2017, 2022; Kremer et al. 2017; Lamberts et al. 2019; Breivik et al. 2020; Li et al. 2020). *LISA* will also be sensitive enough to observe several tens to hundreds of DWDs harboured in Milky Way satellite galax-

ies (Korol et al. 2018, 2020; Roebber et al. 2020). UCBs with neutron stars and/or stellar-mass black holes are also expected to be detected, although in much smaller numbers (Hils et al. 1990; Nelemans et al. 2001; Lamberts et al. 2018; Andrews et al. 2020; Lau et al. 2020; Wagg et al. 2022).

Since the population of short-period UCBs is so abundant, the systems that *LISA* can resolve will just be the ‘tip of the iceberg’. The incoherent superposition of GWs from the remaining unresolved sources in this population will produce a stochastic foreground signal, known as a confusion noise (Hils et al. 1990; Ruiter et al. 2010; Farmer & Phinney 2003; Georgousi et al. 2022). This confusion noise will actually dominate over *LISA*’s instrumental noise in the frequency region $\sim 0.5\text{--}3$ mHz.

Uniquely among GW sources, DWDs are also bright and persistent sources of electromagnetic (EM) radiation (however, we note that the identification of EM emission from massive black hole binaries might also be expected by the time *LISA* flies; Xin & Haiman 2021). This means that in some cases they can be detected and studied before the launch of *LISA*. In the early 1990s, a few UCBs were already known to be guaranteed GW sources for *LISA* (see, for example, Danzmann et al. 1993; Bender et al. 1998, and references therein). Known UCBs whose radiation will be detectable by future GW missions such as *LISA* are called verification binaries (VBs) (this idea goes back to, e.g., Phinney et al. 2001). VBs offer a guaranteed detection of GWs

* E-mail: efinch@star.sr.bham.ac.uk

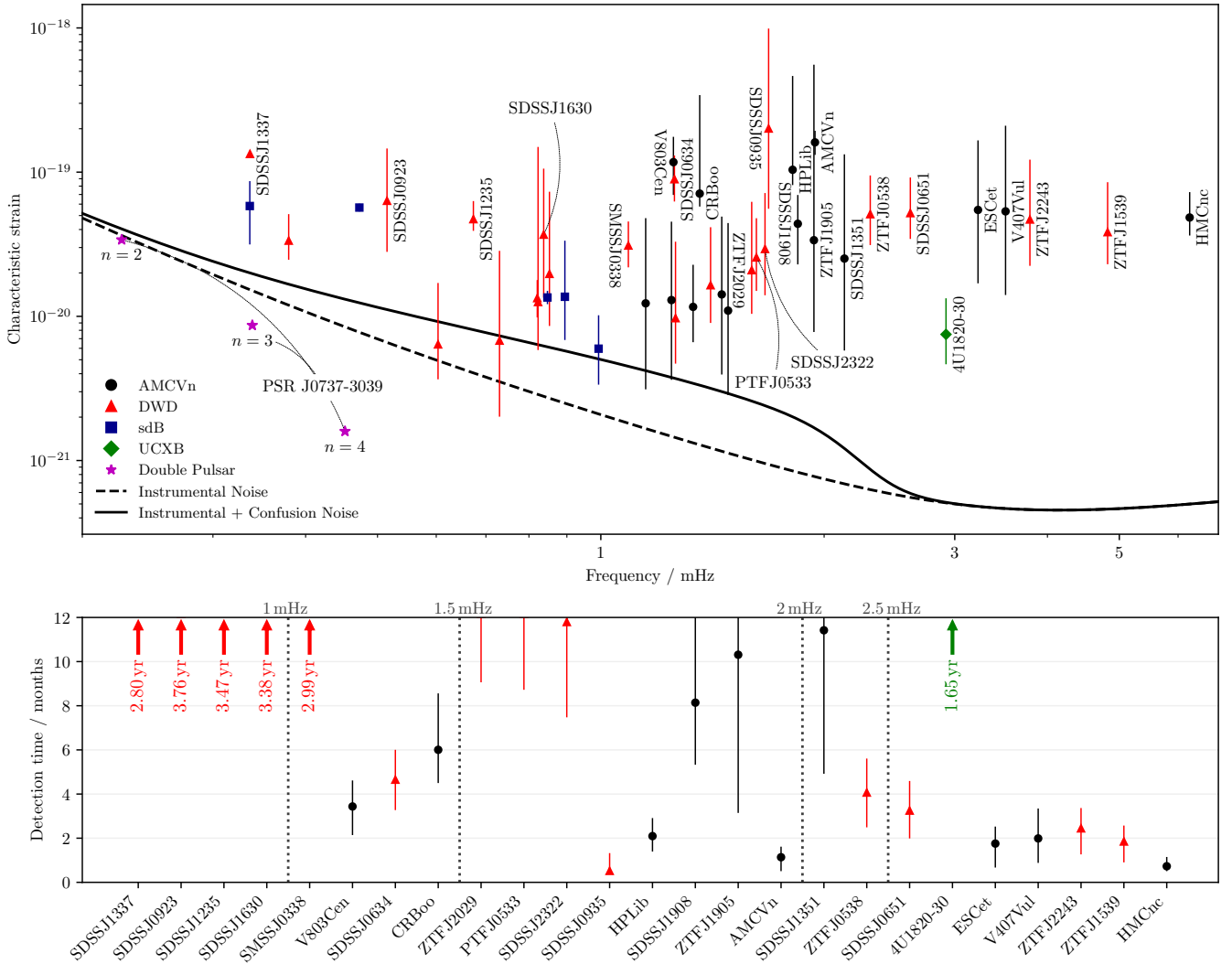


Figure 1. *Top:* The characteristic strain, h_c , of all 43 VB candidates considered in this study (and the double pulsar). This is compared to the *LISA* instrumental noise $\sqrt{f} S_{\text{inst}}$ and to the total noise including the foreground confusion $\sqrt{f} (S_{\text{inst}} + S_{\text{conf}})$ for a mission duration of $T_{\text{obs}} = 4$ yr. The ratio $h_c / \sqrt{f} (S_{\text{inst}} + S_{\text{conf}})$ gives the SNR of the source. Here, we use an SNR calculated in the low-frequency limit, averaged over *LISA* orbital modulations and polarisation angle; further details can be found in Appendix. A. Error bars indicate the full range of possible h_c given the measurement uncertainties in VB component masses, distances, inclinations, and frequencies (these sources of uncertainty being in decreasing order of significance). Also shown are the first few harmonics of the double pulsar PSR J0737-3039 that is on an eccentric orbit with a period of 2.45 h; although it is close, this is not expected to be detectable with *LISA* (see Section 2.2). *Bottom:* Time to detection for the 25 VBs that satisfy $\text{SNR}_{4\text{yr}} > 6$ (i.e., the 25 sources that are detectable within a 4 yr mission). Markers and error bars show the median and 50% error bars on the detection time, including both the astrophysical uncertainty and the *LISA* orbital uncertainty as described in Section 2.3. Sources are shown in order of increasing frequency from left to right. Sources that will not be detectable in the first year of *LISA* science operations are indicated with arrows, and their approximate detection time is shown. We emphasise that no VB sources with frequencies $f_0 < 1$ mHz are expected to be detectable within the first year of *LISA* operations.

within the first few weeks of the *LISA* mission and will be useful for testing the *LISA* instrument and maximising its scientific output. They also offer a new opportunity to study the astrophysics of compact binaries using both their GW and EM emission (e.g. Marsh 2011).

The list of known VBs has grown over the years (Stroeer & Vecchio 2006; Kupfer et al. 2018; Kupfer et al. 2023). New and interesting systems are continuously being discovered by surveys such as the Extremely Low Mass Survey (Brown et al. 2010; Brown et al. 2020a), ATLAS (Tonry et al. 2018), OmegaWhite (Macfarlane et al. 2015), *Gaia* (Prusti et al. 2016) and the Zwicky Transient Facility (ZTF; Bellm et al. 2019; Graham et al. 2019). Their number will increase

further with new surveys such as SDSS-V (Kollmeier et al. 2017), BlackGEM (Bloemen et al. 2015), the Gravitational-wave Optical Transient Observer (Steeghs 2017), and the Vera Rubin Observatory (Ivezic et al. 2019). It is reasonable to expect that the number of known VBs may reach $O(10^3)$ by the time *LISA* flies (e.g. Korol et al. 2017).

An early study of how well *LISA* could measure VB properties was performed by Stroeer & Vecchio (2006), who identified approximately eight VBs above a signal-to-noise ratio (SNR) detection threshold of five and that are therefore expected to be resolvable. Later, Kupfer et al. (2018) used updated EM observations to identify

16 VBs above a similar SNR threshold. Both of these studies used a Fisher matrix formalism to estimate the measurement uncertainties, and both studies used a simplified model for the *LISA* response to GWs involving just two noise-orthogonal channels.

This work represents an update to these previous studies on VBs, making use of the most recent version of the detectable Galactic binaries table from Kupfer et al. (2021, 2023). We also use a realistic model for the *LISA* response to GWs, incorporating all three time-delay interferometry (TDI) output channels and an instrumental noise curve associated with the latest design requirements for the *LISA* mission (Babak et al. 2021). Details of all 43 VB candidates considered in this study are summarised in Table 1, and the top panel of Fig. 1 illustrates the characteristic strain of this set of VBs alongside the chosen *LISA* noise curve. Note that we refer to the full set of binaries considered as “VB candidates”, since not all of them will be detectable in *LISA*. Those sources that satisfy the detection criteria are then known as VBs.

The scope of the study presented here is quite broad, and to help guide the reader we present a summary of the key sections below:

- Section 2, “*Updated VB parameter estimation study*”, contains an updated parameter estimation study on how well the VB properties can be measured from GW observations alone. In this section each VB is considered in isolation and the instrumental noise properties are assumed to be known perfectly. We also study how the SNR for each VB accumulates over time, with a particular focus on the early months of the *LISA* mission so we can estimate the time to detection of the loudest VBs.
- Section 3, “*EM – GW synergies*”, investigates the effect of incorporating EM priors in the GW analysis to address how the accuracy of the measurements can be improved (this complements Johnson et al. 2021, who considered the influence that *LISA* measurements will have on the analysis of EM observations).
- Section 4, “*Accounting for unknown noise levels*”, re-performs the VB parameter estimation study, but now treats the noise in each *LISA* TDI channel as an unknown parameter to be inferred from the data simultaneously with the VB properties. This shows that the results in Section 2 are robust to the addition of uncertain levels of instrumental or confusion noise.
- Section 5, “*Accounting for source confusion*”, performs an analysis of a single typical VB while including all other DWD signals from a realistic Galaxy realisation (predicted from population synthesis). This involves modelling above-threshold (but EM-dark) sources nearby in frequency to the VB, while simultaneously accounting for the below-threshold sources (which constitute the confusion foreground) via a variable noise level.

2 UPDATED VERIFICATION BINARY PARAMETER ESTIMATION STUDY

Table 1 summarises the properties of the currently known candidate VBs split into four sub categories: detached DWDs, accreting DWDs (also known as AM CVns), hot subdwarfs with a white dwarf companion (sdBs), and ultra-compact X-ray binaries (UCXBs). The orbital periods of these binaries are typically well determined from the source variability via photometry or spectroscopy. Component masses are harder to measure because of the intrinsic faintness and the compact configuration (e.g., see Jiménez-Esteban et al. 2018; Rebassa-Mansergas et al. 2019). It is especially difficult for AM

CVn type sources because only the accretion disc and, more exceptionally, the accretor are visible in the spectra. Typically, both component masses can be estimated for eclipsing systems. Distance is yet another parameter difficult to derive from EM observations. For many VBs, distance could be derived thanks to the arrival of the *Gaia* data, which was considered in Kupfer et al. (2018). Here we use up-to-date distance estimates derived in Kupfer et al. (2023) based on the latest *Gaia* data release 3. We note, however, that the highest frequency binary (HMCnc) – expected to be the ‘loudest’ *LISA* source among currently known Galactic binaries – in the sample is lacking parallax measurement; as a consequence, its distance remains highly uncertain. As in Kupfer et al. (2023), for HMCnc we consider a range of possible distances between 5 and 10 kpc, which comprises various estimates in the literature. Finally, we note that the inclination is a degenerate parameter that can generally only be well constrained for eclipsing or nearly eclipsing systems.

2.1 GW parameter estimation

We use the up-to-date candidate VB properties in Table 1 and a Bayesian inference pipeline to study the measurement of the VB source properties from their GW signals alone. We emphasise that we do not use any prior EM-derived knowledge on the GW parameters in the analyses in this section; a study of the improvement obtained with a combined multimessenger analysis is left to Section 3.

Bayesian parameter estimation was performed using the BALROG code (Roebber et al. 2020; Buscicchio et al. 2021; Klein et al. 2022). BALROG simulates the *LISA* mission, including DWD waveform generation and the *LISA* response with mock noise, and has the capability to perform parameter estimation. Unlike ground-based detectors, the *LISA* data can be processed to produce three output channels (conventionally named *A*, *E*, and *T*) containing independent noise. With the additional assumptions of stationarity and Gaussianity, the noise in each channel can be characterised by the power spectral density (PSD) and we write the likelihood as a product over the three independent channels as

$$P(d|h) \propto \prod_{\alpha} \exp\left(-\frac{1}{2}\langle d-h|d-h\rangle_{\alpha}\right), \quad (1)$$

where *h* and *d* are the frequency-domain representations of the signal model and observed data respectively in the three TDI channels: $\alpha = A, E, \text{ and } T$. The inner product in each channel is defined as

$$\langle a|b\rangle_{\alpha} = 2 \sum_k \frac{a_k b_k^* + a_k^* b_k}{S_{\alpha}(f_k)} \delta f, \quad (2)$$

where $S_{\alpha}(f_k)$ is the PSD in channel α . All quantities are in the frequency domain and the subscript *k* indexes the frequency components in their discrete Fourier transforms. The frequency resolution is $\delta f = 1/T_{\text{obs}}$.

The optimal SNR over an observation time T_{obs} is defined as a sum over all three TDI channels

$$\text{SNR}_{T_{\text{obs}}} = \left[\sum_{\alpha} \langle h|h\rangle_{\alpha} \right]^{1/2}, \quad (3)$$

and is used to determine whether a particular VB can be detected. The SNR increases with mission duration T_{obs} , but not in the usual $\propto \sqrt{T_{\text{obs}}}$ manner. The rate at which the SNR accumulates is complicated by the Galactic confusion noise (see Appendix A) that decreases over time as it becomes possible to individually resolve more of the UCB sources in the Galaxy. This means the effective noise PSD decreases for longer mission durations, thereby raising the SNR. This

Table 1. Source properties measured from EM observations for the set of known VBs (accessed on 2022 September 2) from Kupfer et al. (2021) (see also Kupfer et al. 2023). Masses, distances, and inclination angles with no available uncertainty information are quoted to two significant figures, and values stated in square brackets represent indirect estimates based on theoretical arguments (Kupfer et al. 2018). We note that HMCnc has an essentially unconstrained distance, and in the parameter estimation study in Section 2 below we adopt the median (7500 pc) of the stated range as our fiducial value; we note that this differs from the value used in Kupfer et al. (2018), although see the discussion in Section 5 of that paper. Inclinations are only in the range 0–90 deg due to the inability of EM observations to distinguish between an inclination of x degrees and $(180 - x)$ degrees. GW observations from *LISA* will resolve this degeneracy and find the true inclination of each system in the range 0–180 deg. (Note that when injecting VBs we choose to inject with the inclination given in the table.) Eclipsing systems are denoted with *.

Type Source	l / deg	b / deg	P / s	m_1 / M_\odot	m_2 / M_\odot	D / pc	i / deg	Refs.
AMCVn								
HMCnc	120.4387	-4.7040	321.5291290(10)	0.55	0.27	[5000 – 10000]	38	1, 2, 3
V407Vul	-65.0093	46.7833	569.39623(13)	[0.80 ± 0.10]	[0.177 ± 0.071]	2090 ± 680	[60]	2
ESCet *	24.6080	-20.3339	620.21125(30)	[0.80 ± 0.10]	[0.161 ± 0.064]	1780 ± 230	[60]	4
SDSSJ1351	-151.6161	4.4721	939.0 ± 7.2	[0.80 ± 0.10]	[0.100 ± 0.040]	1530 ± 760	[60]	5
AMCVn	170.3818	37.4426	1028.73220(30)	0.680 ± 0.060	0.125 ± 0.012	302.0 ± 3.0	43.0 ± 2.0	6
SDSSJ1908	-61.7867	61.4542	1085.1080(10)	[0.80 ± 0.10]	[0.085 ± 0.034]	977 ± 32	15.0 ± 5.0	7, 8
HPLib	-124.9155	4.9599	1102.700(50)	0.65 ± 0.15	0.07 ± 0.20	280.0 ± 3.0	30.0 ± 4.0	9, 10
PTF1919 *	-51.0016	69.0291	1347.354(20)	[0.80 ± 0.10]	[0.066 ± 0.026]	1360 ± 470	[60]	11
CX1751	-91.9424	-6.2528	1374.00(60)	[0.80 ± 0.10]	[0.064 ± 0.026]	1130 ± 260	[60]	12
CRBoo	-157.7309	17.8971	1471.306(50)	0.89 ± 0.21	0.07 ± 0.22	351.0 ± 5.0	30	10, 13
V803Cen	-143.8365	-30.3168	1596.4 ± 1.2	0.97 ± 0.20	0.084 ± 0.025	287.0 ± 5.0	13.5 ± 1.5	10, 14
KLDra	-25.8709	78.3217	1501.806(30)	0.76	0.057	930 ± 91	[60]	15
PTF0719	104.3844	26.5213	1606.2 ± 1.2	[0.80 ± 0.10]	[0.053 ± 0.021]	840 ± 200	[60]	16
CPEri	42.1289	-26.4276	1740(84)	[0.80 ± 0.10]	[0.049 ± 0.020]	750 ± 200	[60]	17
ZTFJ1905 *	-66.2000	53.6764	1032.16441(62)	[0.80 ± 0.10]	[0.090 ± 0.035]	700 ± 600	70 ± 20	18
DWD								
SDSSJ0651 *	101.3338	5.8064	765.206543(55)	0.247 ± 0.013	0.490 ± 0.020	960 ± 370	86.9 ^{+1.6} _{-1.0}	19, 20
SDSSJ0935	130.9744	28.0938	1188(42)	0.312 ± 0.019	0.75 ± 0.24	400 ± 200	[60]	21, 22
SDSSJ1630	-128.2284	63.0527	2388.0 ± 6.0	0.298 ± 0.019	0.76 ± 0.24	850 ± 170	[60]	21, 23
SDSSJ0923	133.7104	14.4288	3884(43)	0.275 ± 0.011	0.76 ± 0.23	288.0 ± 5.0	[60]	21, 24
ZTFJ1539 *	-154.9724	66.1616	414.7915404(29)	0.610 ^{+0.017} _{-0.022}	0.210 ± 0.015	2500 ± 1300	84.15 ^{+0.64} _{-0.57}	18
ZTFJ0538 *	84.8261	-3.4567	866.60331(16)	0.450 ± 0.050	0.320 ± 0.030	1000 ± 370	85.430 ^{+0.070} _{-0.090}	18
PTFJ0533	82.9058	-21.1234	1233.97298(17)	0.652 ^{+0.037} _{-0.040}	0.167 ± 0.030	1170 ± 390	72.8 ^{+0.8} _{-1.4}	18
ZTFJ2029 *	-45.5630	33.4339	1252.056499(41)	0.320 ± 0.040	0.300 ± 0.040	1100 ± 640	86.64 ^{+0.70} _{-0.40}	18
ZTFJ1749 *	-92.9622	32.8224	1586.03389(44)	0.400 ^{+0.070} _{-0.050}	0.280 ^{+0.050} _{-0.040}	2000 ± 1200	85.5 ^{+1.4} _{-1.1}	18
ZTFJ2243 *	13.2384	53.9599	527.934890(32)	0.349 ^{+0.093} _{-0.074}	0.38 ^{+0.11} _{-0.07}	1760 ± 730	81.9 ^{+1.3} _{-0.7}	25
SDSSJ2322	-6.5666	8.4572	1201.4 ± 5.9	0.340 ± 0.020	>0.17	860 ± 210	[60]	26
SDSSJ1235	-178.2132	17.9524	2970.4 ± 4.3	0.350 ± 0.010	0.270 ^{+0.060} _{-0.020}	446 ± 28	27.0 ± 3.8	27
ZTFJ0722	115.8862	-40.2651	1422.548655(71)	0.380 ± 0.040	0.330 ± 0.030	1460 ± 780	89.66 ± 0.22	18
ZTFJ1901	-53.1907	74.6334	2436.10817(93)	0.360 ± 0.040	0.360 ± 0.050	909 ± 78	87.28 ± 0.50	18
SMSSJ0338	80.4851	59.4015	1836(32)	0.230 ± 0.015	0.380 ^{+0.050} _{-0.030}	536 ± 16	69.0 ± 9.0	28
SDSSJ0634	97.0793	14.8391	1591(29)	0.452 ^{+0.070} _{-0.062}	0.209 ^{+0.034} _{-0.021}	433 ± 16	37.0 ± 7.0	28
SDSSJ1337	-177.1107	45.5716	5942.95(30)	0.510 ± 0.010	0.320 ± 0.010	113.78 ± 0.57	13.0 ± 1.0	29
ZTFJ2320	8.7132	38.0937	3314.7998(40)	0.690 ± 0.030	0.200 ± 0.010	1480 ± 860	84.5 ^{+2.7} _{-3.2}	18
SDSSJ1043	160.1506	-2.0480	2739(79)	0.183 ± 0.010	0.76 ± 0.25	2800 ± 1200	[60]	30
SDSSJ0822 *	120.6776	11.0965	2430.07250(10)	0.304 ± 0.014	0.524 ± 0.050	1300 ± 1200	87.70 ± 0.20	31
SDSSJ0106	11.4543	-15.7928	2345.8 ± 1.7	0.188 ± 0.011	0.57 ^{+0.22} _{-0.07}	820 ± 440	67 ± 13	32
WD0957	-151.4766	-67.3014	5269.810804(73)	0.370 ± 0.020	0.320 ± 0.030	163.70 ± 0.80	75 ± 15	33
sdB								
CDm30 *	-138.8255	-16.6150	4231.79186(15)	0.540 ± 0.020	0.790 ± 0.010	355.0 ± 7.0	82.900 ± 0.040	34
ZTFJ2130 *	-11.8355	54.4443	2360.4062(14)	0.545 ± 0.020	0.337 ± 0.015	1307 ± 42	86.4 ± 1.0	18
HD265435	101.3348	10.1443	5945.91743(28)	0.63 ^{+0.13} _{-0.12}	1.01 ± 0.15	461 ± 12	64 ⁺¹⁴ ₋₅	35
ZTFJ1946	-52.0264	52.0541	2013.82141(75)	0.272 ^{+0.046} _{-0.043}	0.307 ^{+0.097} _{-0.085}	2120 ± 300	77.1 ^{+1.6} _{-1.2}	18
ZTFJ0640	99.6393	-5.4567	2236.0160(16)	0.39 ^{+0.12} _{-0.09}	0.325 ^{+0.030} _{-0.015}	1580 ± 620	65.3 ± 5.1	18
UCXB								
4U1820-30	-84.8589	-7.0267	685.0 ± 4.0	[1.4]	[0.069]	7600	[60]	36

[1] Strohmayer (2005), [2] Barros et al. (2007), [3] Roelofs et al. (2010), [4] Espaillet et al. (2005), [5] Green et al. (2018), [6] Skillman et al. (1999), [7] Fontaine et al. (2011), [8] Kupfer et al. (2015), [9] Patterson et al. (2002), [10] Roelofs et al. (2007b), [11] Levitan et al. (2014), [12] Wevers et al. (2016), [13] Provencal et al. (1997), [14] Roelofs et al. (2007a), [15] Wood et al. (2002), [16] Levitan et al. (2013), [17] Howell et al. (1991), [18] Burdge et al. (2020a), [19] Brown et al. (2011), [20] Hermes et al. (2012), [21] Brown et al. (2016), [22] Kilic et al. (2014), [23] Kilic et al. (2011b), [24] Brown et al. (2010), [25] Burdge et al. (2020b), [26] Brown et al. (2020b), [27] Kilic et al. (2017), [28] Kilic et al. (2021), [29] Chandra et al. (2021), [30] Brown et al. (2017), [31] Kosakowski et al. (2021), [32] Kilic et al. (2011a), [33] Moran et al. (1997), [34] Geier et al. (2013), [35] Pelisoli et al. (2021), [36] Chen et al. (2020)

Table 2. GW-derived parameter estimates for the set of known VBs, with an integration time of 4 yr and an $\text{SNR}_{4\text{yr}} > 6$ detection threshold. For the remaining sources that do not satisfy this detection threshold, we do not report parameter estimates, since they are found to be uninformative. The values $\Delta\mathcal{A}/\mathcal{A}$, f_0 , \dot{f} , and ι are given to a 1σ confidence, and Ω_{90} is the 90% credible region sky localisation.

Type	SNR			$\frac{\Delta\mathcal{A}}{\mathcal{A}}$	f_0 / mHz	\dot{f} / nHz yr ⁻¹	ι / deg	Ω_{90} / deg ²
Source	1 yr	4 yr	10 yr					
AMCVn								
HMCnc	49.1	98.1	155	0.086	6.22027624(18)	23.579 ± 0.087	30 ± 10	0.26
V407Vul	46.4	116	183	0.021	3.51249253(15)	2.602 ± 0.079	59.9 ± 1.0	0.097
ESCet	35.8	115	182	0.021	3.22470771(14)	1.747 ± 0.072	60.1 ± 1.0	0.21
SDSSJ1351	5.39	20.5	55.9	0.18	2.12992548(84)	0.23 ± 0.42	54 ± 14	27
AMCVn	29.9	94.9	288	0.095	1.94414061(18)	0.171 ± 0.084	38 ± 10	0.53
SDSSJ1908	7.68	22.7	67.2	0.15	1.84313450(79)	0.12 ± 0.40	37 ± 13	7.1
HPLib	17.8	51.7	151	0.10	1.81372994(32)	0.08 ± 0.16	31 ± 11	4.9
PTF1919	1.49	3.85	8.18	-	-	-	-	-
CX1751	1.91	4.89	10.2	-	-	-	-	-
CRBoo	8.82	22.0	42.9	0.15	1.35933688(76)	0.05 ± 0.38	38 ± 13	28
V803Cen	13.4	32.7	60.4	0.13	1.25281882(57)	0.04 ± 0.27	34 ± 12	11
KLDra	1.41	3.51	6.73	-	-	-	-	-
PTF0719	1.48	3.61	6.65	-	-	-	-	-
CPEri	1.30	3.09	5.54	-	-	-	-	-
ZTFJ1905	6.28	19.8	60.0	0.085	1.93767579(90)	0.16 ± 0.46	69.4 ± 3.4	9.7
DWD								
SDSSJ0651	15.9	84.0	143	0.012	2.61367341(22)	0.83 ± 0.10	86.90 ± 0.33	1.1
SDSSJ0935	31.2	85.5	222	0.029	1.68350165(21)	0.296 ± 0.097	59.8 ± 1.4	1.0
SDSSJ1630	2.86	6.39	10.8	0.32	0.8375210(31)	0.0 ± 2.3	52 ± 18	470
SDSSJ0923	3.06	6.42	10.4	0.31	0.5149755(33)	0.0 ± 1.8	52 ± 17	1193
ZTFJ1539	41.8	84.1	133	0.012	4.82169908(19)	8.005 ± 0.096	84.15 ± 0.36	0.073
ZTFJ0538	12.4	57.7	128	0.018	2.30786102(31)	0.62 ± 0.15	85.43 ± 0.53	3.2
PTFJ0533	3.78	10.1	24.6	0.21	1.6207811(18)	0.12 ± 0.91	70 ± 12	104
ZTFJ2029	3.15	8.38	19.9	0.14	1.5973720(23)	0.1 ± 1.1	86.2 ± 4.4	116
ZTFJ1749	1.12	2.74	5.09	-	-	-	-	-
ZTFJ2243	47.7	104	164	0.010	3.78834595(18)	3.584 ± 0.088	81.88 ± 0.32	0.091
SDSSJ2322	4.50	12.2	31.2	0.24	1.6647245(15)	0.09 ± 0.72	49 ± 16	93
SDSSJ1235	2.99	6.46	10.7	0.31	0.6733028(29)	0.0 ± 1.7	51 ± 17	960
ZTFJ0722	2.14	5.42	10.9	-	-	-	-	-
ZTFJ1901	1.02	2.28	3.84	-	-	-	-	-
SMSSJ0338	3.08	7.26	12.8	0.31	1.0892653(30)	0.0 ± 1.4	57 ± 17	222
SDSSJ0634	10.2	25.0	46.3	0.14	1.25675506(75)	0.04 ± 0.35	37 ± 13	25
SDSSJ1337	3.61	7.35	11.7	0.26	0.3365330(24)	0.0 ± 1.2	49 ± 16	793
ZTFJ2320	0.358	0.765	1.26	-	-	-	-	-
SDSSJ1043	0.463	1.01	1.69	-	-	-	-	-
SDSSJ0822	0.995	2.22	3.75	-	-	-	-	-
SDSSJ0106	1.57	3.52	5.96	-	-	-	-	-
WD0957	1.09	2.23	3.58	-	-	-	-	-
sdB								
CDm30	2.50	5.21	8.42	-	-	-	-	-
ZTFJ2130	1.06	2.39	4.04	-	-	-	-	-
HD265435	1.59	3.24	5.16	-	-	-	-	-
ZTFJ1946	0.541	1.25	2.17	-	-	-	-	-
ZTFJ0640	1.12	2.54	4.34	-	-	-	-	-
UCXB								
4U1820-30	3.38	14.7	23.6	0.21	2.9197080(13)	0.78 ± 0.60	50 ± 15	34

effect is most pronounced for sources with intermediate frequencies around ~ 2 mHz where the confusion is the dominant source of noise. The rate at which the SNR accumulates is further complicated by the orbital motion of the *LISA* constellation around the Sun. The quadrupolar antenna pattern of *LISA* introduces oscillations in its sensitivity to GWs from a particular sky direction at a frequency of 2 yr^{-1} . These effects can be seen in Fig. 2 where the cumulative SNR of each candidate VB is plotted over a 10 yr mission duration. This is consistent with previous work on the SNR evolution over time (Kupfer et al. 2018; Seoane et al. 2022), which also shows an

SNR scaling that differs from a simple square root dependence. The rate at which the SNR accumulates in the first few months of the *LISA* mission is investigated in more detail in Section 2.3.

The parameter estimation results from the GW-only analysis are summarised in Table 2. *LISA* $\text{SNR}_{T_{\text{obs}}}$ values are reported for mission durations of $T_{\text{obs}} = 1, 4,$ and 10 yr for all 43 candidate VBs. Although parameter estimation analyses were performed for all three mission durations, results in the table are quoted for the *LISA* nominal mission duration of 4 yr (Amaro-Seoane et al. 2017). We find that UCB sources below a threshold SNR of $\lesssim 6$ generally cannot be detected

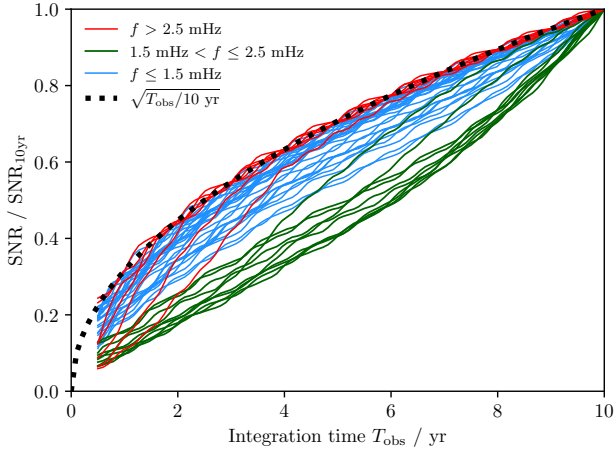


Figure 2. Cumulative SNR of all 43 VB candidates as a function of *LISA* integration time over a 10 yr mission. Sources are coloured in three categories according to their frequency. The dotted black line shows the simple $\text{SNR} \propto \sqrt{T_{\text{obs}}}$ dependence expected for a stationary detector with a constant noise PSD. This is not realised for *LISA* because the confusion noise decreases with time; sources at intermediate frequencies where the confusion is the dominant noise source accumulated SNR approximately linearly in time. The oscillations visible at a frequency of 2 yr^{-1} are due to the orbital motion of the *LISA* constellation.

or characterised by *LISA* (the posteriors are typically broad, with no clear peaks and with an amplitude consistent with zero). Throughout this paper, we adopt a value of $\text{SNR} = 6$ as a fiducial threshold required for detection. Parameter estimation results are only shown in Table 2 for the 25 resolvable sources with $\text{SNR}_{4\text{yr}} > 6$.

Each VB was injected into a zero-noise realisation and analysed individually. The analysis was performed using the likelihood function in Eq. (1) with the noise PSD being the sum of the instrumental noise (as described in the latest *LISA* Science Requirement Document Babak et al. 2021) and the astrophysical confusion noise from the unresolved Galactic binaries (modelled using Eq. A2 from Babak et al. 2017).

Each VB is described by eight parameters: a GW strain amplitude \mathcal{A} , a GW frequency f_0 (equal to twice the binary orbital frequency, $f_0 = 2/P$), a time derivative of GW frequency \dot{f} , an inclination angle ι , an ecliptic latitude and longitude (b, l), and the initial phase ϕ_0 and polarisation angle ψ . The injected values, where possible, are derived from the median EM-observed values in Table 1. The GW strain amplitude is given by (Blanchet 2014)

$$\mathcal{A} = \frac{2(GM_c)^{5/3}(\pi f_0)^{2/3}}{Dc^4}, \quad (4)$$

where $M_c = (m_1 m_2)^{3/5} / (m_1 + m_2)^{1/5}$ is the chirp mass, and D is the distance to the source. For the injection, the frequency derivative was assumed to be driven by GW emission and has the quadrupole-formula-derived value of

$$\dot{f} = \frac{96}{5} \left(\frac{GM_c}{c^3} \right)^{5/3} \pi^{8/3} f_0^{11/3}. \quad (5)$$

This constraint was not used in the recovery where \dot{f} was treated as a free parameter, allowing us to potentially measure the effects of tides or mass transfer on the evolution of the binary. No constraints on the initial phase and polarisation are obtained from the EM observations;

the injected values for these parameters were drawn randomly from the priors.

A blind search was performed for each VB. We emphasise that this analysis is deliberately *not* taking into account what is already known about the VBs from EM observations. The analysis used the following flat priors: $\mathcal{A} \in [0, 10\mathcal{A}_0]$; $f_0 \in [f_0 - 3/T_{\text{obs}}, f_0 + 3/T_{\text{obs}}]$; $\dot{f} \in [-10^{-15}, 10^{-15}] \text{ s}^{-2}$; $\cos(\iota) \in [-1, 1]$; $\sin(b) \in [-1, 1]$; $l \in [0, 2\pi]$; $\phi_0 \in [0, 2\pi]$; $\psi \in [0, \pi]$.

The modular design of the *BALROG* code allows it to be called with a wide range of stochastic samplers. In this paper, the *NES-SAI* (Williams et al. 2021) implementation of the nested sampling algorithm (Skilling 2006) was used to sample the posterior distribution. The runs in this section were performed with 2000 live points and required an average of 967, 2575, and 8026 CPU seconds for the 1, 4, and 10 yr analyses respectively.

We find that, with GW measurements only, we can generally measure the (above-threshold) VB amplitudes to the 1% level, the GW frequency to a subfrequency bin width precision (one part in $\gtrsim 10^5$), and for sources with $f_0 \gtrsim 2 \text{ mHz}$ we can constrain the frequency derivative away from zero.

Compared to the recent study by Kupfer et al. (2018), our analysis includes 12 new (recently discovered) sources that satisfy the chosen resolvability criteria. This includes five ZTF sources (one AMCVn, four DWDs), four SDSS DWDs, the DWDs SMSSJ0338 and PTFJ0533, and the UCXB 4U1820-30. The close-to-threshold sources in Kupfer et al. (2018) (PTF1919, CX1751, and CDm30) do not meet the resolvability criteria used in this study. We see good agreement with the 4 yr SNRs reported in table 3 of Kupfer et al. (2018), with the exception of HMCnc (our SNR is a factor of ~ 2 smaller) and SDSSJ0935 (our SNR is a factor of ~ 2 bigger). These differences are due to choices for the distance to the source. There is also broad agreement with the measurement uncertainties on the VB amplitude and inclination. However, in a few cases we find errors smaller than those previously reported; this is likely to be due to choices for the source distance and differences in the details of the analysis.

Fig. 3 shows the recovered sky positions of the 25 VBs with $\text{SNR}_{4\text{yr}} > 6$. For each VB, the 90% credible GW-recovered sky position is shown along with the injected value (which comes from the EM observations). The GW-derived sky position is consistent with the much more precise EM-derived sky position in all cases. Table 2 also reports the 90% credible GW-recovered sky area Ω_{90} for these sources.

2.2 The double pulsar PSR J0737-3039

The term “verification binary” is used for any *LISA* source that can be observed electromagnetically in advance. These are mostly DWDs but, in principle, can include other compact objects. An example that is tantalisingly close to being within the sensitivity reach of *LISA* is the double pulsar PSR J0737-3039 (Burgay et al. 2003; Lyne et al. 2004). The binary is mildly eccentric, $e = 0.088$, so it radiates GWs at multiple frequency harmonics $f_{\text{GW}} = n/P = n \times 0.113 \text{ mHz}$, where $P = 2.45 \text{ h}$ is the orbital period (see the top panel of Fig. 1). The orbital parameters of this source are known with exquisite accuracy (Kramer et al. 2021) and the expected SNRs in the first few harmonics ($n = 1$ to 6) are 0.01, 1.33, 0.70, 0.20, 0.04, and 0.01 after $T_{\text{obs}} = 10 \text{ yr}$ of *LISA* observations. The total SNR across all harmonics is 1.52. This is too quiet for *LISA* to detect and therefore this is not expected to be a verification source.

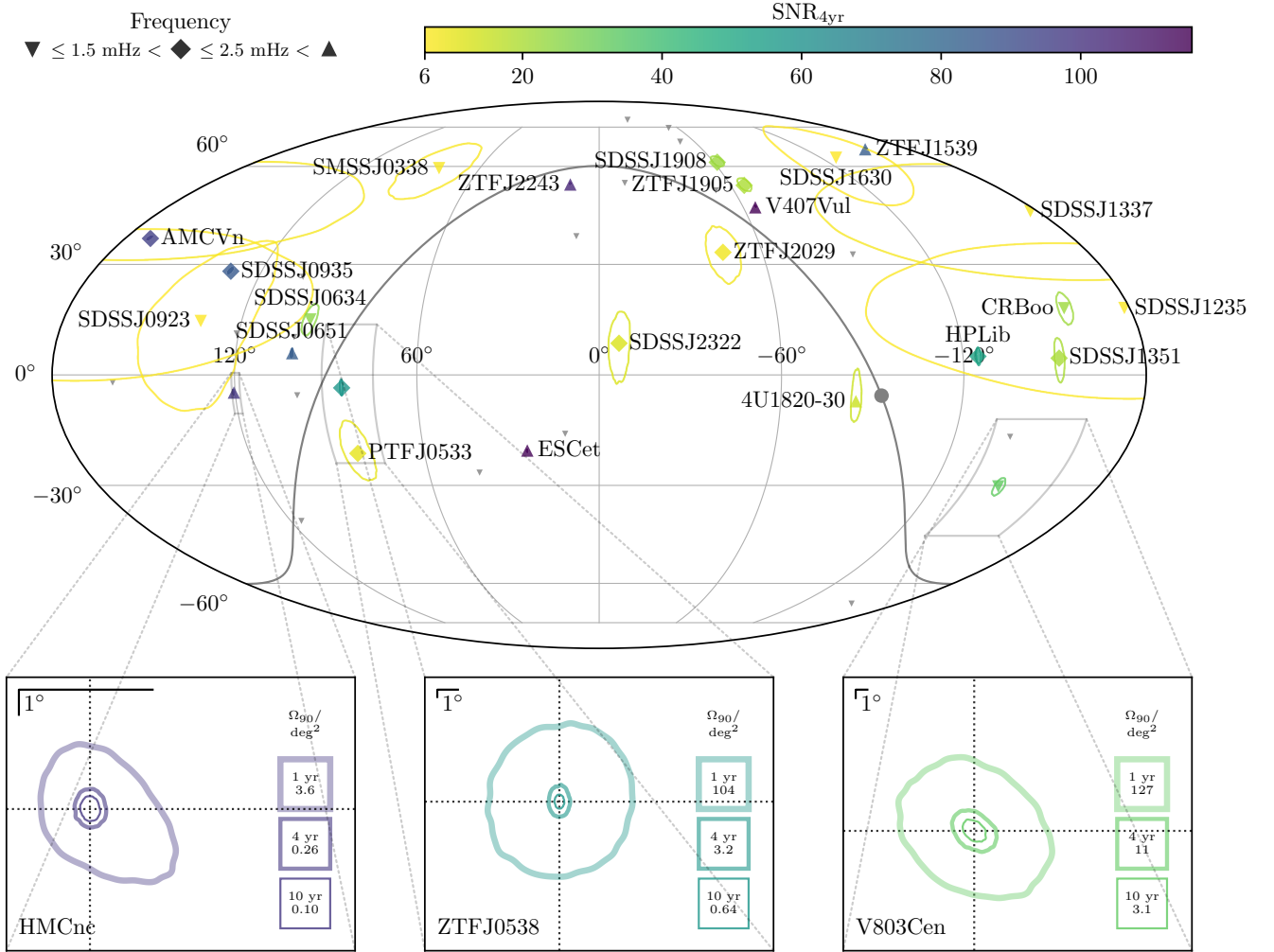


Figure 3. Skymaps of all 43 VB candidates in the ecliptic coordinate frame. Known sky positions (used as the injected values in the analysis) are indicated by markers. The marker shape indicates the VB frequency. For the 25 resolvable VBs satisfying $\text{SNR}_{4\text{yr}} > 6$, the marker colour indicates the VB $\text{SNR}_{4\text{yr}}$. Additionally, for the above-threshold sources, the recovered sky position (90% credible region) after $T_{\text{obs}} = 4$ yr is shown by a contour. For reference, the Galactic equator and centre are indicated by the grey line and marker, respectively. *Insets:* For HMCnc (high f_0), ZTFJ0538 (medium f_0), and V803Cen (low f_0), the recovered sky position is shown for $T_{\text{obs}} = \{1, 4, 10\}$ yr with the associated decreasing areas, Ω_{90} , showing the improvement over time. The scale of each inset is indicated in the top left by 1° lines in both longitude and latitude.

2.3 Verification binaries in the early months of LISA operations

VBs will be key in helping to establish the early performance of the instrument in comparison to pre-launch predictions. This will be particularly important during the first few months of science operations. In turn, this may well play a role in determining the timing and content of the first *LISA* data releases.

To help guide expectations for which and how many VBs might be detectable in the early months of *LISA* science operations, in the top panel of Fig. 4 we show the SNR evolution over the first year of the mission for an illustrative selection of loud VBs. The total number of VB sources that exceed the $\text{SNR} > 6$ detection threshold as a function of mission duration is plotted in the bottom panel.

For the SNR calculations, the GW signals are computed with astrophysical parameters derived from Table 1. Two sources of uncertainty are accounted for in these SNR calculations: astrophysical and orbital. The astrophysical uncertainties arise from the errors on the parameters obtained from EM observations. The orbital uncertainty

reflects the fact that we do not yet know the exact positions of the *LISA* spacecraft at the start of science operations. Over multi-year observations, the size of the orbital uncertainty decreases as the motion of the *LISA* constellation averages over a complete orbit; however, for observation times shorter than a year this is an important extra source of uncertainty.

Fig. 4 accounts for both sources of uncertainty using a Monte Carlo average. The SNR was computed as a function of T_{obs} for a set of 1000 parameter draws (astrophysical and orbital position) for each VB. The astrophysical parameters were drawn either from a Gaussian distribution (for parameters where both the mean and standard deviation are available in Table 1) or from a uniform distribution in cases where parameters are unconstrained (to be conservative, for sources with inclination given as [60] we draw inclination samples uniformly in the range $0-\pi$). The initial orbital position of *LISA* is described by two angles (see, for example, the appendix of Cornish & Rubbo 2003): one describing the phase of the centre of the con-

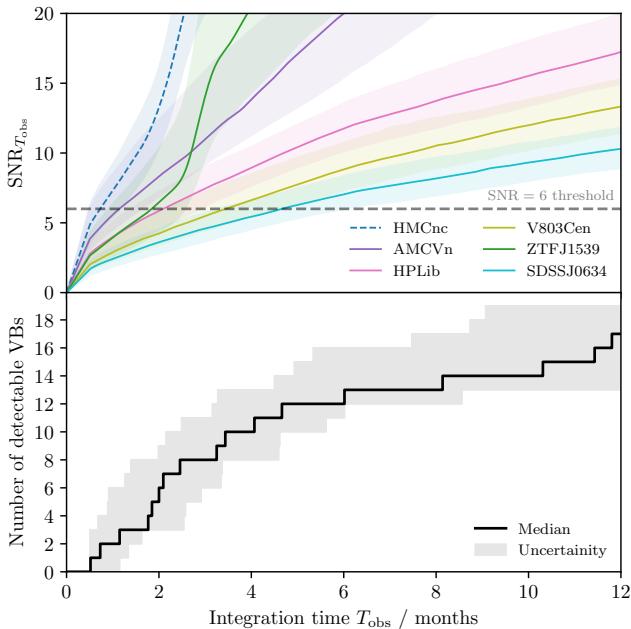


Figure 4. *Top:* Accumulated SNR as a function of mission duration for an illustrative selection of loud VBs. The shaded region for each VB corresponds to the 50% confidence interval, with the uncertainty coming from the astrophysical parameters and *LISA* orbit. We note HMCnc (shown here with a dashed line) has a particularly large uncertainty on its distance; we account for this uncertainty by drawing samples in the range 5–10 kpc. Even with this accounted for, its high frequency means that it is likely to be one of the loudest VBs (which is why we include it here). *Bottom:* Number of VB sources that exceed the detection threshold $\text{SNR} > 6$ as a function of observation time. The shaded region in the bottom panel corresponds to the same 50% confidence interval from the top panel (coming from both the astrophysical and orbital uncertainties). None of the VBs below 1 mHz are detectable within the first year of *LISA* operation, as seen in the bottom panel of Fig. 1.

stellation around the Sun and one describing the orientation of the three spacecraft within the constellation. These angles were drawn uniformly across their full ranges.

The size of the orbital SNR uncertainty is larger than the astrophysical SNR uncertainty at early times, but is smaller for mission durations $T_{\text{obs}} \geq 3$ months. These SNR calculations are assuming that the instrumental noise requirements for the *LISA* mission (Babak et al. 2021) are met exactly, and that the Galactic confusion noise from the unresolved Galactic binaries is described by Eq. (A2) from Babak et al. (2017); in reality, both of these are additional sources of SNR uncertainty.

From Fig. 4, it is expected that two VBs will likely be observable after just 1 month of observations. After 6 (12) months, it is expected that at least 11 (13) VBs will be detectable. Further results for the time to detection for all 25 individual VBs are shown in the bottom panel of Fig. 1, from which one can see that none of the VBs below 1 mHz are expected to be observed before *LISA* gathers ≈ 2.5 yr of data.

3 ELECTROMAGNETIC – GRAVITATIONAL-WAVE SYNERGIES

The analysis in the previous section deliberately did not use any prior EM-derived knowledge of the VB parameters. This information can

be included in the prior of the GW analysis where it may help to confidently detect a VB close to the SNR threshold or improve the parameter estimation accuracy of a louder VB. This section explores the influence of prior knowledge of the frequency (f_0), inclination (ι), and sky location (l, b). The choice of these parameters was motivated by the availability of EM measurements and on expectations from previous (Fisher-matrix) studies (Shah et al. 2012, 2013). The analysis was originally performed on a set of simulations where f_0 , ι , l , and b were separately fixed to the respective EM-measured value. We then analysed the simulations where combinations of these variables were fixed. In order to have clearer results, only the most informative constraints are presented in this section. We illustrate our results with two example VBs: SDSSJ0651 that is nearly edge-on ($\iota = 87$ deg; this gives rise to approximately linearly polarised GWs), and SDSSJ1908 which is nearly face-on ($\iota = 15$ deg; this gives rise to approximately circularly polarised GWs).

For a specific mission duration, five different types of analysis were considered: (1) a blind search (using the uninformative priors from Section 2) and four searches with various parameters fixed to their EM-measured values. These are: (2) frequency fixed, (3) inclination fixed, (4) sky position fixed, and (5) sky position and inclination fixed. Search (4) can be described as a ‘directed’ or ‘targeted’ search.

The effect of a particular prior choice is illustrated by considering its effect on the one-dimensional marginalised posterior on the amplitude, \mathcal{A} . We use the ratio of the mean, μ , and the standard deviation, σ , of this amplitude posterior as a proxy for how confidently a VB source can be detected. At low SNR, the amplitude is consistent with zero and resembles a truncated distribution; this has a ratio $\mu/\sigma \approx 1$, meaning that the VB cannot be detected. At high SNR, the amplitude posterior is peaked away from zero and has a ratio $\mu/\sigma \gg 1$, meaning that the VB can be detected. Empirically, we identify a threshold value of $\mu/\sigma > 2.5$ as being the minimum value necessary to detect a VB source (this corresponds roughly to an SNR of 6).

Fig. 5 shows the evolution of the ratio μ/σ with increasing mission duration for the two example sources. The earliest time at which the source can be detected is when $\mu/\sigma = 2.5$. Compared to the blind search (1), in all other cases (2–5) the effect of including EM prior information is a modest reduction in the time to detection (knowledge of the inclination parameter leads to the biggest reduction). SDSSJ0651 (SDSSJ1908) is detected after 104 d (134 d) with a blind search, 92 d (109 d) with the directed search, and 83 d (91 d) with search (5).

From a Bayesian perspective, the reduction in time to detection with improved prior knowledge is expected and can be explained in terms of the Bayes’ factor and Occam’s razor. Fixing a model parameter to its true value reduces the size of the remaining parameter space, increasing the Bayesian evidence for the signal hypothesis by reducing its associated Occam penalty. The evidence for the null hypothesis is unaffected, so the Bayes’ factor (equal to the ratio of the evidences) increases, making detection easier.

After the source is detected, the two panels of Fig. 5 show different behaviour. For the edge-on source, prior knowledge from EM observations does not significantly affect the amplitude measurement. However, for face-on sources prior knowledge of the inclination angle ι does lead to a dramatic improvement in the amplitude measurement; this improves further for longer observations. For SDSSJ1908, after $T_{\text{obs}} = 2$ yr, prior knowledge of ι leads to an improvement in the amplitude measurement by a factor of 2.4. Similar results were obtained for all the other VBs that were analysed.

From the above discussion, it is clear that prior EM-derived knowledge of the inclination angle is particularly important. The reason for

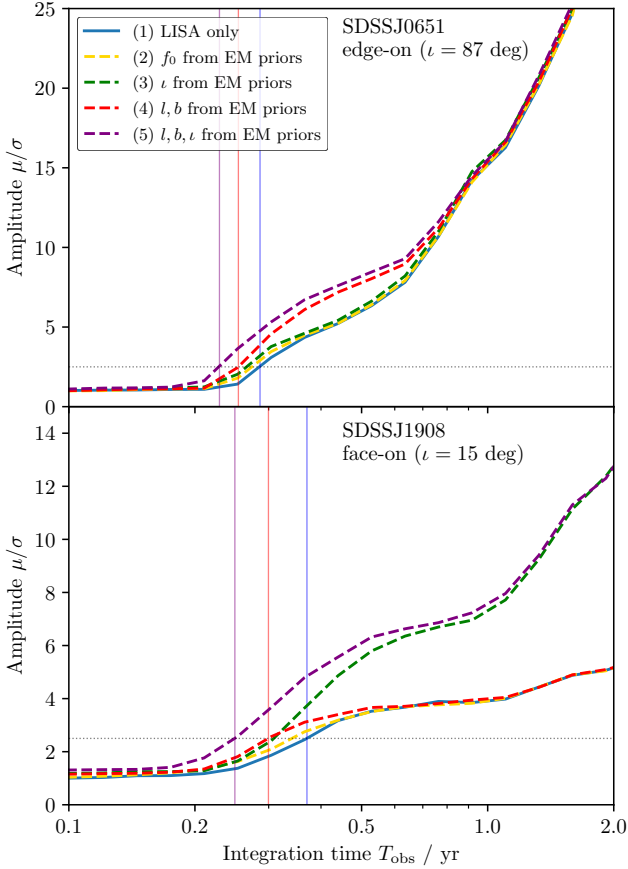


Figure 5. Mean over standard deviation of the amplitude posteriors for the edge-on source SDSSJ0651 (top), and for the face-on source SDSSJ1908 (bottom) as a function of mission duration. The solid blue line shows the results for a blind search (1), while dashed lines show searches with different EM-informed priors (2–5). The horizontal line indicates the detection threshold $\mu/\sigma = 2.5$. Vertical lines show the detection times for the (1), (4), and (5) searches. In both cases, prior knowledge of VB parameters reduces the time to detection. For long T_{obs} , prior knowledge of the inclination for the face-on source leads to a very significant improvement in the posterior.

this can be traced back to the fact that two-dimensional posteriors on \mathcal{A} and ι typically show a strong degeneracy; this is particularly true for nearly face-on or face-off sources. Therefore, fixing the inclination to its true value helps to improve the measurement of the amplitude. The amplitude in turn is related to the component masses and the distance to the source (see Eq. (4)). This is consistent with what was found by Shah et al. (2012) using Fisher matrices.

It should also be noted that the GW measurements can also be used to improve the EM measurements of the inclination angle. Even in cases where the inclination is known from EM observations (see Table 1), it is typically not known in which direction on the sky the VB is orbiting (i.e. an EM-measured inclination of $\iota = 1^\circ$ could correspond to a nearly face-on source seen orbiting in a counterclockwise direction or to a nearly face-off source with $\iota = 179^\circ$ seen orbiting clockwise). GW measurements will break this degeneracy (see results in Table 2). This is consistent with what was found by Littenberg & Cornish (2019) in the specific case of ZTF J1539+5027.

Knowledge of the inclination helps most for face-on systems. However, it is harder to measure ι for such systems because they are not eclipsing. If the inclination is not known but the VB source is known

not to be eclipsing, this implies that the binary is not close to edge-on and therefore places a weak constraint on the inclination. To investigate the usefulness of such a constraint we conducted a post-analysis on all VBs with $\iota = [60^\circ]$ in Table 1. Posterior samples with $85^\circ < \iota < 95^\circ$ were removed, mimicking the effect of a prior that excludes this range of ι that would give rise to eclipses. Unfortunately, the resulting posteriors showed a negligible improvement.

4 ACCOUNTING FOR UNKNOWN NOISE LEVELS

The VB analyses described above all used the standard form of the likelihood, Eq. (1). This assumes that the noise in each independent data time series is additive, stationary, and Gaussian. The statistical properties of this type of noise can be described in terms of the PSD, $S_\alpha(f)$. The standard GW likelihood also assumes that this noise PSD is known exactly beforehand. In reality, the instrumental noise sources will not be understood perfectly and it will also be necessary to account for the presence of the Galactic foreground as an additional uncertain noise source in the analysis. In this section we describe how this can be done as part of a fully Bayesian analysis of VB sources by relaxing the assumption of a known noise PSD.

Hereafter, instead of Eq. (1), we use a modified GW likelihood:

$$P(d|h) = \prod_{\alpha} \frac{\exp\left(-2 \sum_k \frac{|d_{\alpha}(f_k) - h_{\alpha}(f_k)|^2}{(1 + \delta_{\alpha}) S_{\alpha}(f_k)} \delta f\right)}{2\pi \prod_k (1 + \delta_{\alpha}) S_{\alpha}(f_k) \delta f}, \quad (6)$$

where α labels the TDI channel. When the noise is treated as an unknown in the analysis it is necessary to include the denominator of Eq. (6) (see, e.g., Littenberg 2011).

A fixed, reference PSD $S_{\alpha}(f)$ is used in Eq. (6) [although we use the same symbol, we stress that the meaning of $S_{\alpha}(f)$ here is different from that in Eq. (2)]. This can be chosen to be our best *a priori* estimate for the *LISA* noise; this was taken to be the same PSD that was used in Section 2.1, including the estimate of the confusion noise. This is fixed throughout the analysis. However, this reference noise PSD is multiplied by a factor $1 + \delta_{\alpha}$. The three new parameters δ_{α} describe variations in the noise level relative to the *a priori* PSD estimate. These parameters can account for both instrumental and Galactic foreground noise sources. VBs are extremely narrow band sources with GW signal power present only in a few frequency bins; therefore, we choose to use a single parameter in each TDI channel to describe variations in the noise level only (the shape of the PSD is kept fixed). Flat priors were used on the δ_{α} parameters with sufficiently broad ranges that the posteriors are unaffected by prior boundaries.

In Section 5 this likelihood is used to analyse multiple signals simultaneously. First, however, the VB sources were reanalysed individually with this likelihood to ensure they can still be individually detected and characterised in the presence of unknown noise levels. The VBs were injected into simulated *LISA* noise generated from the PSDs shown in Fig. 6 (see also the solid black curve in the top panel of Fig. 1).

Our ability to constrain the PSD δ_{α} parameters depends on how much data are analysed. The sums and products over k in Eq. (6) are taken over a small frequency range centred on the GW frequency of the VB. Because δ_{α} describes the noise level across the whole band, the more frequency bins that are included the better the resulting measurement of δ_{α} . In order to ensure a fair comparison between δ_{α} posteriors from different analyses the number of frequency bins was fixed to 438 in all cases. This value was chosen to be as small as possible while still comfortably containing all the signal power for

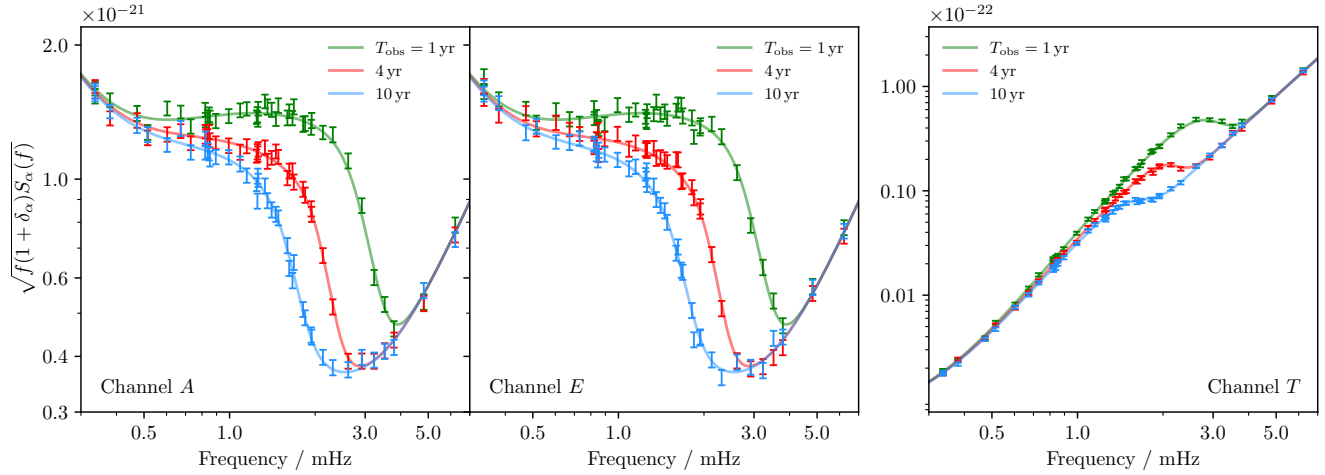


Figure 6. Representative constraints on the noise curve in channels *A*, *E*, and *T*, with mission durations of 1, 4, and 10 yr plotted in blue, orange, and green respectively. Error bars show 90% confidence intervals. Also plotted for comparison is the *LISA* noise PSD used for the injection. At low frequencies the GW signal in the *T* channel is highly suppressed.

all the VB sources (accounting for Doppler broadening and a 10 yr frequency drift for those sources with large \dot{f}). All other details of this analysis are the same as those presented in Section 2.

For each of the 43 VB candidates, two analyses were performed at mission durations of $T_{\text{obs}} = 1, 4,$ and 10 yr: an analysis with known PSDs (all three δ_α parameters fixed to zero) and an analysis with unknown noise levels (δ_α allowed to vary). Notice that even in cases where the VB cannot be detected, it is still possible to measure δ_α . For those VBs above the threshold, we find that it is still possible to detect and characterise them in the presence of unknown noise levels. The recovered posteriors were nearly identical in both simulations for most VBs, with a small number showing a small shift in some parameters, consistent with the width of the posterior.

Two interesting cases were CX1751 after 4 yr and ZTFJ0640 after 10 yr. Here the SNRs were just below threshold, with SNRs of 4.89 and 4.34 respectively. This resulted in VB parameter posteriors that were somewhat constrained when the δ_α were fixed but that became unconstrained when the δ_α were free parameters; posterior information for marginally subthreshold sources can be lost when marginalising over uncertain noise levels.

It is also possible to use these results to gain some insight into our ability to measure the *LISA* noise level. Because the δ_α are treated as free parameters we obtain posterior distributions on these parameters for all 43 VB candidates. Plotted in Fig. 6 are the 90% confidence regions for the reconstructed noise level $\sqrt{f(1+\delta_\alpha)S_\alpha(f)}$ in all three TDI channels. The results are shown for all 43 separate VB candidate analyses on a single plot as a function of frequency. For each VB (and for each T_{obs}) we have single measurement of δ_α . We plot the posterior on the noise curve $\sqrt{f(1+\delta_\alpha)S_\alpha(f)}$. Because we have VBs spread across a range of frequencies, this set of measurements can be used as a crude reconstruction of the full noise PSD across the whole *LISA* band. Because we are analysing VBs one at a time (with no other sources present) and in the presence of simulated Gaussian noise, we expect that the recovered values of δ_α should be consistent with the PSD used for the injection; this can be seen to be the case in Fig. 6. With our choice of number of frequency bins, $N_{\text{bin}} = 438$, the noise curve can be measured to an accuracy of $\approx 8\%$ (90% credible interval). We stress that the magnitude of

the uncertainties on the PSDs shown in Fig. 6 are determined by our choice of N_{bin} and the uncertainty on δ_α scales as $1/\sqrt{N_{\text{bin}}}$. We also stress that we have taken the most conservative approach in which the three noise parameters are treated as independent. Understanding of *LISA*'s subsystem behaviour during mission operation may provide additional constraints across parameters describing the noise.

5 ACCOUNTING FOR SOURCE CONFUSION

Thus far, the VBs have been treated in isolation. This neglects the rest of the GP of UCBs that *LISA* will face, both individually resolved and unresolved. (However, the effects of the unresolved sources are partly accounted for in the model for the Galactic confusion noise.) In this section, we adopt a fiducial mock Galaxy catalogue to directly determine the impact of the rest of the UCBs in the Galaxy on our ability to measure VB parameters.

Here we consider the GP of detached DWDs only, as they are expected to be at least an order of magnitude more numerous than the other types of stellar remnant binaries in *LISA*'s frequency band (Amaro-Seoane et al. 2023). Specifically, we use a mock DWD catalogue from Wilhelm et al. (2020) assembled by combining the DWD binary population synthesis model of Toonen et al. (2012) with a snapshot of GALAKOS, a high-resolution N -body simulation of a stellar disc and bulge/bar with structural parameters that reproduce the currently observed properties of our Galaxy (D'Onghia & L. Aguerri 2020). Representative of a Milky Way-like Galaxy with a total stellar mass of $5 \times 10^{10} M_\odot$, the catalogue contains $\sim 1.4 \times 10^7$ DWDs emitting in the *LISA* frequency band. Based on an SNR criterion, Wilhelm et al. (2020) showed that $\sim 2.2 \times 10^4$ DWDs could be detected within 4 yr of the mission, while the rest would contribute to the Galactic confusion foreground signal.

5.1 Population analysis

First, we attempt to quantify how ‘confused’ each VB source is. This is designed to be a measure of both how many other UCBs are close in frequency to the VBs, and how loud these sources are. A source

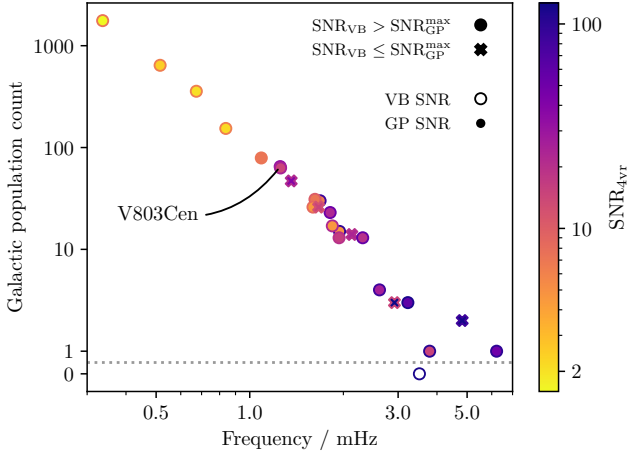


Figure 7. The number of DWDs in a simulated GP (Wilhelm et al. 2020) within 10 frequency bins ($T_{\text{obs}} = 4$ yr) of each VB, after accounting for Doppler broadening (see Eq. 7). These sources will need to be accounted for in a realistic analysis of the VB. Marker fill colour indicates the $\text{SNR}_{4\text{yr}}$ of the loudest member of the GP within the frequency range, while the marker edge colour indicates the $\text{SNR}_{4\text{yr}}$ of the VB. We consider a VB to be more ‘confused’ (i.e. likely to be harder to separate from the rest of the population) if it has more, or louder, DWD sources nearby in frequency. VBs with a circular marker satisfy $\text{SNR}_{\text{VB}} > \text{SNR}_{\text{GP}}^{\text{max}}$, while those with a cross satisfy $\text{SNR}_{\text{VB}} \leq \text{SNR}_{\text{GP}}^{\text{max}}$. The VB V803Cen is highlighted; this is analysed further in Section 5.2.

from the GP is classified as ‘close’ if its frequency f_0^{GP} (accounting for Doppler broadening) crosses into any of the 10 frequency bins (for a 4 yr mission) centred on the VB initial frequency f_0 ; i.e. if

$$\left| f_0^{\text{GP}} - f_0 \right| < 5\delta f + \frac{\nu}{c} f_0, \quad (7)$$

where $\nu/c \approx 10^{-4}$ is the orbital velocity of *LISA* around the Sun. The actual Doppler broadening will depend on the ecliptic latitude of the source; Eq. (7) uses the maximum value. This can be thought of as counting sources from the GP which have power in the 10 closest frequency bins to the VB.

For each VB, members of the GP within the permitted frequency range were counted and their SNRs computed. Note that these SNRs are computed in the same manner as those in Table 2, with respect to the fixed instrumental plus confusion noise curve. Then, the highest SNR among the sources in the GP was identified and compared to the SNR of the VB. This information is summarised in Fig. 7.

As expected, the GP source count is a steeply decreasing function of frequency. In this particular realisation of the Galactic DWD population, the VBs CRBoo, SDSSJ2322, SDSSJ1351, 4U1820-30, and ZTFJ1539 have associated with them at least one DWD with an SNR greater than their own, i.e. $\text{SNR}_{\text{VB}} > \text{SNR}_{\text{GP}}^{\text{max}}$. The case of 4U1820-30 is particularly extreme with the ratio $\text{SNR}_{\text{VB}}/\text{SNR}_{\text{GP}}^{\text{max}} = 0.12$.

All VBs will be confused to some extent, with the possible exception of a few of the highest frequency VBs. In some cases there are thousands of other sources nearby in frequency, including several that are louder than the VB itself. In order to successfully perform a GW analysis of the VB under realistic conditions, it is therefore necessary to account for the presence of other individually resolvable DWDs from the GP (whose number is unknown *a priori*) along with the VB and to marginalise over uncertain levels of the noise in the three TDI channels (to which the quiet unresolved DWDs contribute). Optionally, it is also possible to account for the fact that the VB’s

sky location is known, i.e. to perform a ‘directed search’ for the VB, where the sky position angles l and b are fixed to their known values (given in Table 1). This is the goal of the following section.

5.2 VB inference with a realistic confusion foreground

In this section we take as an example VB the binary V803Cen, and place it in the simulated GP described above. V803Cen has 65 DWDs from the GP nearby in frequency (assessed using the criteria in Eq. 7), two of which have $\text{SNR}_{4\text{yr}} > 6$ (the next loudest has an SNR of 5.01). Therefore, it might be expected that we would need to model these two additional sources to perform reliable inference on the VB.

To demonstrate this, a 4 yr *LISA* data instance was generated including an instrumental noise realisation, the VB V803Cen, plus 229 other DWDs from the (mock) Galaxy. This number includes the 65 sources closest in frequency to the VB, plus the additional sources (in the ~ 100 frequency bins outside the initial frequency range) to ensure we lose no power at the edge of our frequency band used in the analysis.

Using this data instance, we then perform an unknown-noise parameter estimation (using Eq. 6) of the VB while simultaneously modelling N extra sources. The cases $N = [0, 1, 2, 3]$ were explored, and in all cases the VB inference is ‘targeted’ (that is, with fixed sky location) while the other DWDs are searched for over the full sky. The total number of unknown parameters in the analysis is therefore $3 + 6 + (8 \times N)$. All other priors are the same as those described in Section 2.1, with the exception of f_0 which was set to be within the range given by Eq. (7). To deal with the label-switching problem, which arises when multiple sources described by the same model are included in the analysis, we follow the approach in Buscicchio et al. (2019) and order sources by their frequency. All analyses were performed with 4000 live points, and took $\sim 1, 30, 200$ and 500 CPU hours for the $N = 0, 1, 2$, and 3 runs, respectively.

The results are summarised in Fig. 8. In the top right panel of the figure we show the log-Bayes’ factors, $\log_{10} \mathcal{B}_0^N$, comparing the model evidences for different values of N (normalised to the $N = 0$ analysis, i.e. the VB-only analysis). This peaks at $N = 2$ extra sources, consistent with the expectation that only DWDs above a threshold SNR of ~ 6 can be detected. However, the $N = 3$ analysis also has comparable support to the $N = 2$ case (it is disfavoured by $\log_{10} \mathcal{B}_3^2 = 1.2$); we speculate that this is related to the presence of another marginally subthreshold source.

The corner plot in the top half of the figure, with the coloured histograms, shows posteriors on the amplitude, inclination, and frequency for each of the modelled sources in the $N = 2$ analysis. Note that, because of the narrow frequency posteriors, the frequency panels have been split to zoom-in on the posterior for each source. The true (injected) values for each source are shown with the dotted lines. We see posteriors consistent with the injected values for the VB, indicating that we have successfully accounted for the unknown noise and confusion sources. However, only one of the GP sources has posteriors consistent with the injected values. The bias seen in the recovery of GP 1 is a result of our imperfect signal model; the inference on this source is confused by the presence of many other sources (some of which are just below the SNR threshold of 6, and so have not been completely captured by our noise model). Comparing the results to those in Section 2, we see comparable errors in the frequency, amplitude and inclination ($\Delta f/\delta f \sim 0.08$, or one part in 2×10^6 , $\Delta \mathcal{A}/\mathcal{A} \sim 0.15$, $\Delta i \sim 13^\circ$).

To the left of the corner plot are the posteriors on the unknown noise parameters for each TDI channel, δ_α , as described in Section 4. These represent a modification to the instrumental noise curve (no an-

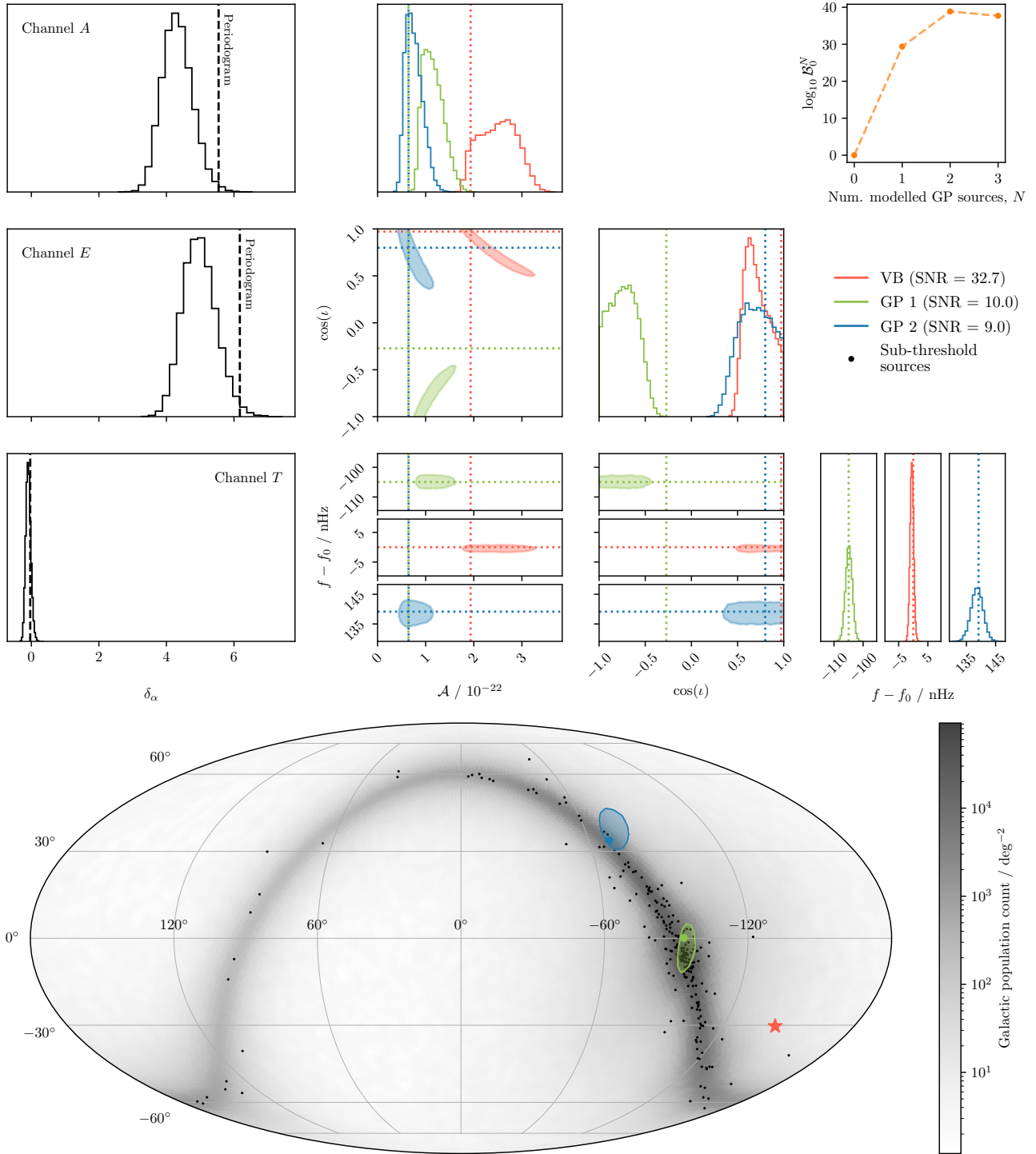


Figure 8. *Top:* Corner plot showing posteriors for V803Cen and two (nearby in frequency) sources from the GP with $\text{SNR}_{4\text{yr}} > 6$, and posteriors on the noise level in each TDI channel with respect to the (design) instrumental noise curve (parameterised through δ_α). A directed search for the VB was performed (shown in red), and blind searches with no prior information for the two Galactic binaries were performed (shown in blue and green). *Bottom:* The skymap of the VB V803Cen (red star) and its associated above-threshold Galactic binaries (blue and green markers), among its subthreshold Galactic binaries (black markers) and the remainder of the mock Galaxy realisation (heatmap). Contours show the recovered sky position (90% credible region) at $T_{\text{obs}} = 4$ yr for the two above-threshold Galactic binaries.

alytical description of the confusion noise is present in this analysis). In the A and E channels, we measure the power from the confusion noise to be $\sim 5 \pm 1$ times greater than the instrumental noise only. The dashed line plotted on each of the histograms indicates an expected value for δ_α , from a periodogram-type calculation. To do this, we generate a new data instance with an instrumental noise realisation and a population of confusion sources (in the same way the data we analysed were created), but we exclude the three modelled sources from the data. In other words, we subtract perfectly the sources we model from the data. With this new data instance, which represents our noise $n^\alpha(f)$, we can calculate the PSD S_α via

$$S_\alpha = \frac{2}{T_{\text{obs}}} \left(|n^\alpha(f)|^2 \right). \quad (8)$$

This approximates the PSD as being constant over the frequency range of the data; as our analysis data are narrow (~ 150 frequency bins, with $T_{\text{obs}} = 4$ yr), this is a reasonable approximation. Finally, to obtain the predicted δ_α , we compare this measured PSD to the instrumental noise curve at the VB frequency f_0 . Our posteriors are broadly consistent with the prediction, but our measurement tends to lower values. One reason for this is that we cannot perfectly model the above threshold sources in our Bayesian analysis. As seen in the other panels of Fig. 8, confusion between the GP sources leads to biases in the posteriors. As we may be “absorbing” power from other (just below threshold) GP sources into our model, this causes an underestimate of the noise. The loudest below-threshold sources may also break the assumption of a constant (in time and frequency) PSD in the application of Eq. (8).

Finally, the bottom panel of the figure shows a skymap with the locations of the VB V803Cen (a targeted sky search, red star), the other two DWDs we model (for which the 90% credible regions are shown with green and blue contours), and the other 227 subthreshold sources from the GP that were included in the data. The heatmap indicates the density of all $\sim 1.4 \times 10^7$ sources in the (mock) Galaxy. We see sky recovery consistent with the injected values.

6 DISCUSSION AND CONCLUSIONS

Unique among GW sources, a small number of Galactic UCBs are known in advance of the operation of a GW observatory as guaranteed sources. Extending previous studies of VBs, e.g. Kupfer et al. (2018), we have considered the most recent list (and relevant parameter errors) of VBs maintained by the LISA Consortium and available at Kupfer et al. (2021) (see also Kupfer et al. 2023), and carried out the work within a Bayesian framework using the three independent TDI channels A , E , and T and the instrument performance according the current science requirements.

We have shown that *LISA* will detect 25 currently known systems over its nominal mission lifetime with SNR in the range ≈ 6 –100. We have also quantified the expected accuracy with which the system parameters will be measured by computing their marginalised posterior probability distributions, and shown that *LISA* will provide astrophysically non-trivial measurements for quantities such as orbital inclination and the evolution of the orbital period. We have also quantified the extent to which prior knowledge of the source parameters affects the integration time required to detect a VB, therefore providing an early “verification” of *LISA*’s performance.

Consistent with previous studies, we have derived these baseline results under the assumption that the noise affecting the measurements is known and that within the frequency band covered by a VB signal no other GW source is present. Both assumptions are clearly

wrong, and one may wonder how reliable these results, as well as all of those present in the literature, actually are. We have therefore generalised our analysis in the two key directions that remove these oversimplifications.

First, we have relaxed the assumption that the noise, both coming from the instrument and from the unresolved foreground of Galactic and extragalactic UCBs, is known in advance. By including the noise level (parameterised by a single parameter in each TDI channel) as one of the parameters that need to be fitted in the analysis, we have shown that there is minimal effect on the accuracy with which the VB parameters can be measured. As a by-product of this analysis, we have demonstrated that the overall PSD in each of the three channels can be measured to $\sim 8\%$, but we stress that this measurement is dependant on the number of frequency bins included in the analysis.

Secondly, we have accounted for the fact that the signal from VBs will overlap with those from many other UCBs in the Galaxy. By considering a state-of-the-art synthetic population of Galactic binaries, we have analysed a small (≈ 1000 nHz) frequency band fitting concurrently for a VB, an unknown number of other DWDs, and the noise level in the three TDI channels. We have shown that the baseline results presented in Table 2 are robust.

The actual analysis of the *LISA* data to identify VBs will need to include additional refinements that we have not considered here. In particular, we have assumed that the noise contribution is Gaussian and stationary throughout the observing time, which we know is not true. For example, the (dominant, in the band of interest for this work) confusion noise level changes during the year due to the *LISA* motion. We have assumed there are no data gaps (which surely will occur), and we have not considered either transients of instrumental or astrophysical nature (e.g. radiation from a loud massive black hole binary) in the frequency band.

ACKNOWLEDGEMENTS

We thank all the developers of the *BALROG* codesuite, including those who are not authors here. We also thank Thomas Kupfer for maintaining an up-to-date table of *LISA* VBs that has been adopted for our study. Computational resources used for this work were provided by the University of Birmingham’s BlueBEAR High Performance Computing facility. AK, HM, CJM, and AV acknowledge the support of the UK Space Agency, Grant No. ST/V002813/1. AV acknowledges the support of the Royal Society and Wolfson Foundation.

DATA AVAILABILITY

A data release with all posterior samples, SNR calculations, and code to reproduce figures is available at Finch et al. (2022).

REFERENCES

- Amaro-Seoane P., et al., 2017, *arXiv e-prints*, p. arXiv:1702.00786
- Amaro-Seoane P., et al., 2023, *Living Rev. Rel.*, 26, 2
- Andrews J. J., Breivik K., Pankow C., D’Orazio D. J., Safarzadeh M., 2020, *Astrophys. J. Lett.*, 892, L9
- Babak S., et al., 2017, *Phys. Rev. D*, 95, 103012
- Babak S., Hewitson M., Petiteau A., 2021, *arXiv e-prints*, p. arXiv:2108.01167
- Barros S. C. C., et al., 2007, *Mon. Not. Roy. Astron. Soc.*, 374, 1334
- Bellm E. C., et al., 2019, *PASP*, 131, 018002
- Bender P. L., et al., 1998, Technical Report Report MPQ 233, LISA Pre-Phase A Report, 2nd edition. Max-Planck-Institut für Quantenoptik

- Blanchet L., 2014, *Living Rev. Rel.*, 17, 2
- Bloemen S., Groot P., Nelemans G., Klein-Wolt M., 2015, in Rucinski S. M., Torres G., Zejda M., eds, *Astronomical Society of the Pacific Conference Series Vol. 496, Living Together: Planets, Host Stars and Binaries*. p. 254
- Breivik K., et al., 2020, *Astrophys. J.*, 898, 71
- Brown W. R., Kilic M., Allende Prieto C., Kenyon S. J., 2010, *Astrophys. J.*, 723, 1072
- Brown W. R., Kilic M., Hermes J. J., Allende Prieto C., Kenyon S. J., Winget D. E., 2011, *Astrophys. J. Lett.*, 737, L23
- Brown W. R., Kilic M., Kenyon S. J., Gianninas A., 2016, *Astrophys. J.*, 824, 46
- Brown W. R., Kilic M., Kosakowski A., Gianninas A., 2017, *Astrophys. J.*, 847, 10
- Brown W. R., et al., 2020a, *ApJ*, 889, 49
- Brown W. R., Kilic M., Bédard A., Kosakowski A., Bergeron P., 2020b, *Astrophys. J. Lett.*, 892, L35
- Burdge K. B., et al., 2020a, *Astrophys. J.*, 905, 32
- Burdge K. B., et al., 2020b, *Astrophys. J. Lett.*, 905, L7
- Burgay M., et al., 2003, *Nature*, 426, 531
- Buscicchio R., Roebber E., Goldstein J. M., Moore C. J., 2019, *Phys. Rev. D*, 100, 084041
- Buscicchio R., Klein A., Roebber E., Moore C. J., Gerosa D., Finch E., Vecchio A., 2021, *Phys. Rev. D*, 104, 044065
- Chandra V., et al., 2021, *Astrophys. J.*, 921, 160
- Chen W.-C., Liu D.-D., Wang B., 2020, *Astrophys. J. Lett.*, 900, L8
- Cornish N. J., Rubbo L. J., 2003, *Phys. Rev. D*, 67, 022001
- Cutler C., 1998, *Phys. Rev. D*, 57, 7089
- D'Onghia E., L. Aguerra J. A., 2020, *ApJ*, 890, 117
- Danzmann K., et al., 1993, Technical Report Report MPQ 177, Proposal for a Laser-Interferometric Gravitational Wave Detector in Space. Max-Planck-Institut für Quantenoptik
- Espallat C., Patterson J., Warner B., Woudt P., 2005, *Publ. Astron. Soc. Pac.*, 117, 189
- Farmer A. J., Phinney E. S., 2003, *Mon. Not. Roy. Astron. Soc.*, 346, 1197
- Finch E., et al., 2022, Data release for "Identifying LISA verification binaries amongst the Galactic population of double white dwarfs", doi:10.5281/zenodo.7211349, <https://doi.org/10.5281/zenodo.7211349>
- Fontaine G., et al., 2011, *Astrophys. J.*, 726, 92
- Geier S., et al., 2013, *Astron. Astrophys.*, 554, A54
- Georgousi M., Karnesis N., Korol V., Pieroni M., Stergioulas N., 2022, *Mon. Not. Roy. Astron. Soc.*, 519, 2552
- Graham M. J., et al., 2019, *Publ. Astron. Soc. Pac.*, 131, 078001
- Green M. J., et al., 2018, *Mon. Not. Roy. Astron. Soc.*, 477, 5646–
- Hermes J. J., et al., 2012, *Astrophys. J. Lett.*, 757, L21
- Hils D., Bender P. L., Webbink R. F., 1990, *ApJ*, 360, 75
- Howell S. B., Szkody P., Kreidl T. J., Dobrzycka D., 1991, *Publ. Astron. Soc. Pac.*, 103, 300
- Ivezic v., et al., 2019, *Astrophys. J.*, 873, 111
- Jiménez-Esteban F. M., Torres S., Rebassa-Mansergas A., Skorobogatov G., Solano E., Cantero C., Rodrigo C., 2018, *MNRAS*, 480, 4505
- Johnson P. T., et al., 2021, *arXiv e-prints*, p. arXiv:2112.00145
- Karnesis N., Babak S., Pieroni M., Cornish N., Littenberg T., 2021, *Phys. Rev. D*, 104, 043019
- Kilic M., et al., 2011a, *Mon. Not. Roy. Astron. Soc.*, 413, L101
- Kilic M., Brown W. R., Hermes J. J., Allende Prieto C., Kenyon S. J., Winget D. E., Winget K. I., 2011b, *Mon. Not. Roy. Astron. Soc.*, 418, 157
- Kilic M., Brown W. R., Gianninas A., Hermes J. J., Allende Prieto C., Kenyon S. J., 2014, *Mon. Not. Roy. Astron. Soc.*, 444, L1
- Kilic M., Brown W. R., Gianninas A., Curd B., Bell K. J., Allende Prieto C., 2017, *Mon. Not. Roy. Astron. Soc.*, 471, 4218
- Kilic M., Brown W. R., Bedard A., Kosakowski A., 2021, *Astrophys. J. Lett.*, 918, L14
- Klein A., et al., 2022, *arXiv e-prints*, p. arXiv:2204.03423
- Kollmeier J. A., et al., 2017, *arXiv e-prints*, p. arXiv:1711.03234
- Korol V., Rossi E. M., Groot P. J., Nelemans G., Toonen S., Brown A. G. A., 2017, *Mon. Not. Roy. Astron. Soc.*, 470, 1894
- Korol V., Koop O., Rossi E. M., 2018, *Astrophys. J. Lett.*, 866, L20
- Korol V., et al., 2020, *Astron. Astrophys.*, 638, A153
- Korol V., Hallakoun N., Toonen S., Karnesis N., 2022, *Mon. Not. Roy. Astron. Soc.*, 511, 5936
- Kosakowski A., Kilic M., Brown W., 2021, *Mon. Not. Roy. Astron. Soc.*, 500, 5098
- Kramer M., et al., 2021, *Phys. Rev. X*, 11, 041050
- Kremer K., Breivik K., Larson S. L., Kalogera V., 2017, *Astrophys. J.*, 846, 95
- Kupfer T., et al., 2015, *Mon. Not. Roy. Astron. Soc.*, 453, 483
- Kupfer T., et al., 2018, *Mon. Not. Roy. Astron. Soc.*, 480, 302
- Kupfer T., et al., 2021, LISA Verification Binaries, <https://gitlab.in2p3.fr/LISA/lisa-verification-binaries>
- Kupfer T., et al., 2023, *arXiv e-prints*, p. arXiv:2302.12719
- Lamberts A., et al., 2018, *Mon. Not. Roy. Astron. Soc.*, 480, 2704
- Lamberts A., Blunt S., Littenberg T. B., Garrison-Kimmel S., Kupfer T., Sanderson R. E., 2019, *Mon. Not. Roy. Astron. Soc.*, 490, 5888
- Lau M. Y. M., Mandel I., Vigna-Gómez A., Neijssel C. J., Stevenson S., Sesana A., 2020, *Mon. Not. Roy. Astron. Soc.*, 492, 3061
- Levitán D., et al., 2013, *Mon. Not. Roy. Astron. Soc.*, 430, 996
- Levitán D., et al., 2014, *Astrophys. J.*, 785, 114
- Li Z., Chen X., Chen H.-L., Li J., Yu S., Han Z., 2020, *ApJ*, 893, 2
- Lipunov V. M., Postnov K. A., Prokhorov M. E., 1987, *A&A*, 176, L1
- Littenberg T. B., 2011, *Phys. Rev. D*, 84, 063009
- Littenberg T. B., Cornish N. J., 2019, *Astrophys. J. Lett.*, 881, L43
- Lyne A. G., et al., 2004, *Science*, 303, 1153
- Macfarlane S. A., Toma R., Ramsay G., Groot P. J., Woudt P. A., Drew J. E., Barentsen G., Eisloffel J., 2015, *MNRAS*, 454, 507
- Marsh T. R., 2011, *Class. Quant. Grav.*, 28, 094019
- Moran C., Marsh T. R., Bragaglia A., 1997, *Mon. Not. Roy. Astron. Soc.*, 288, 538
- Nelemans G., Yungelson L. R., Portegies Zwart S. F., 2001, *Astron. Astrophys.*, 375, 890
- Nelemans G., Yungelson L. R., Portegies Zwart S. F., 2004, *Mon. Not. Roy. Astron. Soc.*, 349, 181
- Nissanke S., Vallisneri M., Nelemans G., Prince T. A., 2012, *Astrophys. J.*, 758, 131
- Patterson J., et al., 2002, *Publ. Astron. Soc. Pac.*, 114, 65
- Pelisolì I., et al., 2021, *Nature Astron.*, 5, 1052
- Phinney E. S., et al., 2001, LISA Science Requirements, Presentation to the LISA International Science Team, https://lisa.nasa.gov/archive2011/Documentation/LISTwg1_req-pr.pdf
- Provencal J. L., et al., 1997, *Astrophys. J.*, 480, 383
- Prusti T., et al., 2016, *Astron. Astrophys.*, 595, A1
- Rebassa-Mansergas A., Toonen S., Korol V., Torres S., 2019, *Mon. Not. Roy. Astron. Soc.*, 482, 3656
- Roebber E., et al., 2020, *Astrophys. J. Lett.*, 894, L15
- Roelofs G. H. A., Groot P. J., Nelemans G., Marsh T. R., Steeghs D., 2007a, *Mon. Not. Roy. Astron. Soc.*, 379, 176
- Roelofs G. H. A., Groot P. J., Benedict G. F., McArthur B. E., Steeghs D., Morales-Rueda L., Marsh T. R., Nelemans G., 2007b, *Astrophys. J.*, 666, 1174
- Roelofs G. H. A., Rau A., Marsh T. R., Steeghs D., Groot P. J., Nelemans G., 2010, *Astrophys. J. Lett.*, 711, L138
- Ruiter A. J., Belczynski K., Benacquista M., Larson S. L., Williams G., 2010, *Astrophys. J.*, 717, 1006
- Seoane P. A., et al., 2022, *Gen. Rel. Grav.*, 54, 3
- Shah S., van der Sluys M., Nelemans G., 2012, *Astron. Astrophys.*, 544, A153
- Shah S., Nelemans G., van der Sluys M., 2013, *Astron. Astrophys.*, 553, A82
- Skilling J., 2006, *Bayesian Analysis*, 1, 833
- Skillman D. R., Patterson J., Kemp J., Harvey D. A., Fried R. E., Retter A., Lipkin Y., Vanmunster T., 1999, *Publ. Astron. Soc. Pac.*, 111, 1281
- Steeeghs D., 2017, *Nature Astronomy*, 1, 741
- Stroer A., Vecchio A., 2006, *Class. Quant. Grav.*, 23, S809
- Strohmayr T. E., 2005, *Astrophys. J.*, 627, 920
- Tonry J. L., et al., 2018, *PASP*, 130, 064505
- Toonen S., Nelemans G., Portegies Zwart S., 2012, *Astron. Astrophys.*, 546, A70

- Wagg T., Broekgaarden F. S., de Mink S. E., van Son L. A. C., Frankel N., Justham S., 2022, *Astrophys. J.*, 937, 118
- Wevers T., et al., 2016, *Mon. Not. Roy. Astron. Soc.*, 462, L106
- Wilhelm M. J. C., Korol V., Rossi E. M., D’Onghia E., 2020, *Mon. Not. Roy. Astron. Soc.*, 500, 4958
- Williams M. J., Veitch J., Messenger C., 2021, *Phys. Rev. D*, 103, 103006
- Wood M. A., Casey M. J., Garnavich P. M., Haag B., 2002, *Mon. Not. Roy. Astron. Soc.*, 334, 87
- Xin C., Haiman Z., 2021, *Mon. Not. Roy. Astron. Soc.*, 506, 2408

APPENDIX A: NOISE CURVES AND CHARACTERISTIC STRAIN

This appendix gives details of the *LISA* instrumental and confusion noise sources. This appendix also gives useful equations for predicting the SNR of DWD sources computed in a low-frequency approximation. These equations were used to produce the results in the top panel of Fig. 1. We stress that elsewhere in the paper all SNRs were computed using the full *LISA* TDI outputs described in the main text, *without* making a low-frequency approximation.

In the top panel of Fig. 1, the instrumental noise curve is plotted as $s_{\text{inst}}(f) = \sqrt{f S_{\text{inst}}(f)}$, with $S_{\text{inst}}(f)$ being the low-frequency approximation of the PSD in line with the latest SciRD document (Babak et al. 2021):

$$S_{\text{inst}}(f) = (4S_{\text{disp}}(f) + S_{\text{opt}}(f)) \left(1 + 0.6 \left(\frac{2\pi f 2.5 \times 10^9}{c} \right)^2 \right), \quad (\text{A1})$$

with $S_{\text{disp}}(f)$ being the displacement noise and $S_{\text{opt}}(f)$ being the optical noise.

The total noise curve is plotted as $s_n(f) = \sqrt{f S_n(f)}$, where $S_n(f) = S_{\text{inst}}(f) + S_{\text{conf}}(f)$, and the expression for the confusion noise PSD $S_{\text{conf}}(f)$ is obtained from Babak et al. (2017):

$$S_{\text{conf}}(f) = A_{\text{gal}} \left(\frac{f}{1 \text{ Hz}} \right)^{-7/3} \exp \left[- \left(\frac{f}{s_1} \right)^\alpha \right] \times \frac{1}{2} \left[1 + \tanh \left(- \frac{f - f_0}{s_2} \right) \right], \quad (\text{A2})$$

where the parameters A_{gal} , α , s_1 , f_0 , and s_2 were fitted for different values of the observation time (Babak, private communication) and then interpolated as a function of T_{obs} . Note that an updated confusion noise curve can be found in (Karnesis et al. 2021).

The binaries considered here are nearly monochromatic, and emit at low frequencies with respect to the instrumental transfer frequency $f^* = c/2\pi L \approx 19$ mHz, where L is the length of the *LISA* laser arms. Therefore, for the sensitivity estimates used in the top panel of Fig. 1, the signal is modelled in the low-frequency approximation (Cutler 1998). The combined signal is equivalent to two independent detectors, with

$$h_{I,II}(t) = \frac{\sqrt{3}}{2} \left[F_+^{I,II}(t) h_+(t) + F_\times^{I,II}(t) h_\times(t) \right], \quad (\text{A3})$$

$$h_+(t) = -\mathcal{A}(1 + \cos^2 \iota) \cos[2\pi f_0(t - \hat{\mathbf{k}} \cdot \mathbf{P}) + \phi_0], \quad (\text{A4})$$

$$h_\times(t) = 2\mathcal{A} \cos \iota \sin[2\pi f_0(t - \hat{\mathbf{k}} \cdot \mathbf{P}) + \phi_0], \quad (\text{A5})$$

where $F_{+,\times}^{I,II}(t)$ are the detector antenna pattern functions and $c\mathbf{P}$ is the position of *LISA*’s barycentre. The parameter f_0 is the GW frequency of the signal, ϕ_0 is its initial phase, ι is its inclination, $\hat{\mathbf{k}}$ is the wave propagation vector, and \mathcal{A} is the GW strain amplitude given by Eq. (4). The combined squares SNR ρ^2 for this signal is

$$\rho^2 = 4 \int_0^\infty \frac{|\tilde{h}_I(f)|^2 + |\tilde{h}_{II}(f)|^2}{S_n(f)} df. \quad (\text{A6})$$

We can model the antenna pattern functions in the following way (Cutler 1998):

$$F_+^I(t) = \frac{1}{2} \left(1 + \cos^2 \bar{\theta} \right) \cos 2\bar{\phi} \cos 2\bar{\psi} - \cos \bar{\theta} \sin 2\bar{\phi} \sin 2\bar{\psi}, \quad (\text{A7})$$

$$F_\times^I(t) = \frac{1}{2} \left(1 + \cos^2 \bar{\theta} \right) \cos 2\bar{\phi} \sin 2\bar{\psi} + \cos \bar{\theta} \sin 2\bar{\phi} \cos 2\bar{\psi}, \quad (\text{A8})$$

$$F_+^{II}(t) = \frac{1}{2} \left(1 + \cos^2 \bar{\theta} \right) \sin 2\bar{\phi} \cos 2\bar{\psi} + \cos \bar{\theta} \cos 2\bar{\phi} \sin 2\bar{\psi}, \quad (\text{A9})$$

$$F_\times^{II}(t) = \frac{1}{2} \left(1 + \cos^2 \bar{\theta} \right) \sin 2\bar{\phi} \sin 2\bar{\psi} - \cos \bar{\theta} \cos 2\bar{\phi} \cos 2\bar{\psi}, \quad (\text{A10})$$

where $\bar{\theta}$ and $\bar{\phi}$ are the spherical angles of the source position in a frame rotating together with *LISA*’s arms, and $\bar{\psi}$ is a polarisation angle. We can find $\bar{\theta}$ and $\bar{\phi}$ as:

$$\cos \bar{\theta} = \hat{\mathbf{N}} \cdot \hat{\mathbf{z}}, \quad (\text{A11})$$

$$\tan \bar{\phi} = \frac{\hat{\mathbf{N}} \cdot \hat{\mathbf{y}}}{\hat{\mathbf{N}} \cdot \hat{\mathbf{x}}}, \quad (\text{A12})$$

where $\hat{\mathbf{N}}$ is a unit vector pointing towards the source, and $\hat{\mathbf{x}}$, $\hat{\mathbf{y}}$, $\hat{\mathbf{z}}$ form a triad defining the detector frame, given in an inertial frame tied to the ecliptic by

$$\hat{\mathbf{N}} = (\cos b \cos l, \cos b \sin l, \sin b), \quad (\text{A13})$$

$$\hat{\mathbf{x}} = \left(\frac{1}{4} (3 - \cos 2\omega t), -\frac{1}{4} \sin 2\omega t, \frac{\sqrt{3}}{2} \cos \omega t \right), \quad (\text{A14})$$

$$\hat{\mathbf{y}} = \left(-\frac{1}{4} \sin 2\omega t, \frac{1}{4} (3 + \cos 2\omega t), \frac{\sqrt{3}}{2} \sin \omega t \right), \quad (\text{A15})$$

$$\hat{\mathbf{z}} = \left(-\frac{\sqrt{3}}{2} \cos \omega t, -\frac{\sqrt{3}}{2} \sin \omega t, \frac{1}{2} \right), \quad (\text{A16})$$

where b and l are respectively the ecliptic latitude and longitude of the source, and $\omega = 2\pi/\text{yr}$ is the orbital angular frequency of the *LISA* constellation around the Sun.

In order to compute the Fourier transform of the signal, we can take advantage of the fact that the GW frequency f_0 is well separated from the frequency of the modulation from *LISA*’s motion and compute it in a time interval $1/f_0 \ll \Delta T \ll 2\pi/\omega$. We can write

$$\tilde{h}_{I,II}(f) = \sum_{n=0}^{T_{\text{obs}}/\Delta T - 1} \tilde{h}_{I,II}(f, n), \quad (\text{A17})$$

$$\tilde{h}_{I,II}(f, n) = \int_{n\Delta T}^{(n+1)\Delta T} h_{I,II}(t) e^{-2\pi i f t} dt \quad (\text{A18})$$

$$\approx \frac{\sqrt{3}}{2} B_+^{I,II}(n\Delta T) \int_{n\Delta T}^{(n+1)\Delta T} h_+(t) e^{-2\pi i f t} dt + \frac{\sqrt{3}}{2} B_\times^{I,II}(n\Delta T) \int_{n\Delta T}^{(n+1)\Delta T} h_\times(t) e^{-2\pi i f t} dt$$

$$= \frac{\sqrt{3}}{4} [A_+ B_+^{I,II}(n\Delta T) - i A_\times B_\times^{I,II}(n\Delta T)] \times \{g[(n+1)\Delta T] - g(n\Delta T)\}, \quad (\text{A19})$$

$$B_+^{I,II}(t) = F_+^{I,II}(t) e^{-2\pi i f_0 \hat{\mathbf{k}} \cdot \mathbf{P}(t)}, \quad (\text{A20})$$

$$B_\times^{I,II}(t) = F_\times^{I,II}(t) e^{2\pi i f_0 \hat{\mathbf{k}} \cdot \mathbf{P}(t)}, \quad (\text{A21})$$

$$g(t) = \frac{\sin[\pi(f - f_0)t]}{\pi(f - f_0)} e^{-i\pi(f - f_0)t + i\phi_0} + \frac{\sin[\pi(f + f_0)t]}{\pi(f + f_0)} e^{-i\pi(f + f_0)t - i\phi_0}. \quad (\text{A22})$$

Note that since the square SNR in Eq. (A6) is obtained by integrating

over positive frequencies and since this Fourier transform has narrow support, we can neglect the second line in $g(t)$.

Since the pre-factor varies slowly, if the observation window comprises an integer number of years, we can average the pre-factor in this result and obtain the approximation

$$\langle |\tilde{h}_{I,II}(f)|^2 \rangle_t \approx \frac{3I^{I,II}}{16} \frac{\sin^2[\pi(f-f_0)T_{\text{obs}}]}{\pi^2(f-f_0)^2}, \quad (\text{A23})$$

$$I^{I,II} = \int_0^{T_{\text{obs}}} \left(A_+^2 F_+^{I,II}(t)^2 + A_{\times}^2 F_{\times}^{I,II}(t)^2 + 2A_+ A_{\times} F_+^{I,II}(t) F_{\times}^{I,II}(t) \sin[4\pi f_0 \hat{\mathbf{k}} \cdot \mathbf{P}(t)] \right) dt, \quad (\text{A24})$$

where we assumed that the pre-factor in $\tilde{h}_{I,II}(f)$ is a constant equal to its root modulus square average, and simplified the factors of $g(t)$ by taking advantage of the fact that it is then a telescoping sum. We can further average over the polarisation angle $\tilde{\psi}$ to get

$$\langle \rho^2 \rangle_{t,\tilde{\psi}} = 4 \int_0^{\infty} \frac{\langle |\tilde{h}_I(f)|^2 + |\tilde{h}_{II}(f)|^2 \rangle_{t,\tilde{\psi}}}{S_n(f)} df. \quad (\text{A25})$$

The support of $g(T_{\text{obs}})$ as a function of frequency is of the order of a few $\Delta f = 1/T_{\text{obs}}$. Assuming that the noise PSD $S_n(f)$ is constant inside a window of a width of a few Δf around f_0 , we can compute:

$$\langle \rho^2 \rangle_{t,\tilde{\psi}} \approx \frac{3\mathcal{A}^2 T_{\text{obs}}}{4096 S_n(f_0)} \left(443 - 78 \sin^2 b - 37 \sin^4 b \right) \times \left(1 + 6 \cos^2 \iota + \cos^4 \iota \right). \quad (\text{A26})$$

We can similarly compute the SNR averaged over ecliptic latitude and/or inclination. We find

$$\langle \rho^2 \rangle_{t,\tilde{\psi},\iota} \approx \frac{3\mathcal{A}^2 T_{\text{obs}}}{1280 S_n(f_0)} \left(443 - 78 \sin^2 b - 37 \sin^4 b \right), \quad (\text{A27})$$

$$\langle \rho^2 \rangle_{t,\tilde{\psi},b} \approx \frac{3\mathcal{A}^2 T_{\text{obs}}}{10 S_n(f_0)} \left(1 + 6 \cos^2 \iota + \cos^4 \iota \right), \quad (\text{A28})$$

$$\langle \rho^2 \rangle_{t,\tilde{\psi},b,\iota} \approx \frac{24\mathcal{A}^2 T_{\text{obs}}}{25 S_n(f_0)}. \quad (\text{A29})$$

In order to represent the SNR of each VB as a ratio h_c/s_n , the characteristic strain is evaluated with the following formula:

$$h_c = \mathcal{A} \left[\frac{3f_0 T_{\text{obs}}}{4096} (443 - 78 \sin^2 b - 37 \sin^4 b) (1 + 6 \cos^2 \iota + \cos^4 \iota) \right]^{1/2}, \quad (\text{A30})$$

where $T_{\text{obs}} = 4 \text{ yr}$ and $[f_0, b, \iota]$ are the EM measurements of frequency, ecliptic latitude and inclination of the VB respectively (see Table 1). The error bars in the top panel of Fig. 1 on each h_c are the result of the evaluation of the minimum and maximum characteristic strain, obtained by replacing $[f_{\text{min}}, D_{L\text{max}}, m_{1\text{min}}, m_{2\text{min}}, f(t)_{\text{max}}]$ and $[f_{\text{max}}, D_{\text{min}}, m_{1\text{max}}, m_{2\text{max}}, f(t)_{\text{min}}]$ respectively into Eq. (A30). $f(t)$ refers to the expression $f(t) = 1 + 6 \cos^2 \iota + \cos^4 \iota$. The minimum and maximum values of each parameter are reported in Table 1.

This paper has been typeset from a \LaTeX file prepared by the author.